

## Effects of nuclear correlations on low-energy pion charge-exchange scattering

E. R. Siciliano\*

*Department of Physics and Astronomy, University of Georgia, Athens, Georgia 30602  
and Los Alamos National Laboratory, Los Alamos, New Mexico 87545*

M. D. Cooper, Mikkel B. Johnson, and M. J. Leitch

*Los Alamos National Laboratory, Los Alamos, New Mexico 87545*

(Received 3 February 1986)

An isospin-invariant optical-potential framework is used to make a coordinated analysis of low-energy pion elastic and single- and double-charge-exchange scattering to isobaric analog states. The form of the potential studied here is motivated by the work of Stricker, McManus, and Carr, who emphasized the importance of isoscalar absorption-dispersive and correlation effects for low-energy pion elastic scattering. In this paper we examine the influence of the corresponding isovector and isotensor nuclear correlations on low-energy charge exchange. Comparison of our results to 50 MeV data supports the existence of the isovector correlation terms, but shows a need for an additional isotensor effect. A distorted-wave Born approximation analysis confirms that distortions are weak (the mean density of interaction is roughly 50% of the central value), but demonstrates that distortions of the pion waves by the nuclear medium cannot be neglected in describing charge exchange.

### I. INTRODUCTION

New opportunities for learning about pion-nucleus dynamics have become available with the acquisition of recent low-energy pion-nucleus single charge-exchange<sup>1</sup> and double charge-exchange<sup>2</sup> data. The new data complement the elastic scattering measurements at those energies that were taken in the recent past. Interest in low-energy scattering stems from the fact that the pion-nucleon interaction is relatively weak. Consequently, the pion is able to penetrate deeper into the nucleus than at higher energies, where the interaction is much stronger due to the  $\Delta_{33}$  resonance. One may, therefore, hope to learn from measurements both about the distribution of matter at the center of the nucleus and about pion dynamics in high-density nuclear matter.

Low energy pion-nucleus studies have experienced a long history of development. The earliest theoretical work was that of Ericson and Ericson,<sup>3</sup> followed by more specific studies of pionic atoms.<sup>4</sup> Already at this time it was clear that the effective pion-nucleon interaction inside the nucleus is modified by the presence of other nucleons. The physics of short-range and Pauli correlations, and the genuine (or true) absorption of a pion by two nucleons were identified as two of the relevant issues.

With the availability of low-energy elastic scattering data at the new generation of meson factories, interest in the subject was renewed. The theory was extended in a series of papers beginning with Thies<sup>5</sup> and culminating in the work of Stricker, McManus, and Carr<sup>6</sup> at Michigan State University (MSU). (We shall refer to their work as the MSU potential.) The MSU results confirm the earlier conclusions that modifications of the pion-nucleon interaction are needed in order to increase the isoscalar  $s$ -wave repulsion and decrease the isoscalar  $p$ -wave attraction. In the MSU analysis, these effects are essentially at-

tributed to nuclear correlations.

Because of the many different types of physics that enter into the theoretical description of low-energy scattering, it is very useful to find new ways to test these ideas. The low-energy measurements of pion single charge-exchange (SCX) (Ref. 1) and double charge-exchange (DCX) (Ref. 2) scattering to isobaric analog states appear to provide the needed data. The results have distinctive features that could help resolve some of the controversial aspects<sup>7-9</sup> of the role of correlations in the existing theory and that have raised new issues, such as whether quark degrees of freedom<sup>10</sup> in nuclei can be detected directly. The remarkable features of the data are (1) the strong cancellation between  $s$  and  $p$  waves that leads to a forward-angle minimum in the *free* pion-nucleon SCX cross section appears to be preserved when the pion scatters from a nucleus,<sup>1,11,12</sup> and (2) DCX cross sections are large near 50 MeV compared to those at resonance.<sup>2</sup>

The recent charge-exchange data have generated a number of new lines of theoretical investigations, in the framework of the isobar-hole model<sup>13</sup> and the "three-body" approach to pion scattering.<sup>14</sup> In the present work, we examine low-energy pion elastic, SCX, and DCX data in an isospin-invariant optical-potential framework<sup>15,16</sup> that has been successfully applied at resonance energy.<sup>17</sup> In this approach, the isospin-related processes of elastic, SCX, and DCX scattering (collectively referred to as *isoelastic* scattering) are unified. Because the theory permits simultaneous calculation of all three isoelastic reactions, and is identical in form to the MSU theory for elastic scattering, we believe it is suitable for looking at low-energy charge exchange. The nuclear-medium modifications in the elastic and charge exchange channels enter through coefficients in a density expansion. It was shown in a previous paper<sup>15</sup> how these coefficients could be related to the

underlying dynamics for resonance energy scattering. For this case, the coefficients themselves had only weak  $N$ ,  $Z$ , and  $A$  dependence, permitting a relatively simple characterization of large numbers of pion-nucleus cross sections and separation of the dependence of the theory on nuclear structure and reaction dynamics. A subsidiary issue in the current work is whether a simple representation is also possible at low energy. It is conceivable that the increased penetrability of the pion and the nonlocalities intrinsic to low-energy scattering would reduce the accuracies of the approximations. However, we find the MSU model, extended according to the theory of Ref. 16, can successfully describe isoelastic scattering at low energy without modification of its form.

Because the density-dependence of the pion-nucleus interaction is central to this work, we also look at the physics by making a distorted wave Born approximation (DWBA) for low-energy charge exchange. We find this an excellent approximation to the isospin invariant coupled-channel model, and it gives us a clear picture of where in the nucleus the interactions are likely to occur. The DWBA also enables us to make Coulomb corrections and to study explicitly the crucial interplay between the distortions of the initial and final pion waves and the medium modifications to the transition operator.

The outline of the paper is as follows: In Sec. II, we discuss the formulation of the isospin-invariant optical-model approach. This section is divided into two subsections. In the first, we present the general content of the isospin-invariant approach, which does not depend on any specific choice of optical potential. In the second, we focus on the details of the specific optical potential chosen for study in this paper. Because the inclusion of  $p$ -wave correlations in low-energy optical potentials has been somewhat controversial, we devote Sec. III exclusively to the discussion of our model for these effects. In Sec. IV, we present numerical results of our isospin-invariant model for 50 MeV pion-nucleus isoelastic scattering. We introduce, in Sec. V, a DWBA for charge exchange, and we study in detail the separate effects of distortions and nuclear-medium modifications to the reaction mechanism for SCX. In Sec. VI, we summarize our findings and draw our conclusions. A synopsis of the main points addressed in each section appears in the first few paragraphs of that section, and some of the necessary but tedious manipulations appear in the appendices.

## II. ISOSPIN INVARIANT FORMULATION FOR LOW ENERGY

The isospin-invariant formulation of pion-nucleus scattering is an optical-model approach that explicitly couples the nuclear ground state to the isobaric analog states. The main ingredients of this coupled-channel model are the three isospin components of the optical potential: the isoscalar, isovector, and isotensor potentials. Because pion elastic scattering is most sensitive to the isoscalar potential, and because low-energy elastic scattering has been well studied,<sup>6</sup> we adopt the attitude that the isoscalar component is known. Fixing the isoscalar potential

is also important for the charge-exchange reactions because it essentially determines the distortions that are needed to evaluate correctly pion SCX and DCX. Thus, the central issue for low-energy charge exchange is the study of the corresponding isovector and isotensor potentials. We establish the calculational foundation for such a study in this section.

Our presentation is divided into two subsections. In subsection A, we discuss in general terms the content of the isospin invariant calculational framework and we emphasize certain aspects of this approach that are of particular significance for low energies. Some of the main points discussed in this subsection are the following: (1) The isovector potential, which is fixed by SCX, makes an important contribution to DCX by means of sequential single-charge-exchange transitions via the single isobaric analog state (IAS). We define this as the analog route to DCX. (2) Direct coupling of the ground state (g.s.) to the double isobaric analog state (DIAS), for example by means of nonanalog routes, can be incorporated through the addition of the isotensor potential. (3) Although the Coulomb potential violates our assumption of isospin invariance, we are able to include it in our elastic scattering calculations where it is needed.

In subsection B, we present the specific optical potential we use for our low-energy calculations. The main features of the potential are the following: (1) The first-order terms of the potential (those that are linear in the nuclear density) are explicitly separated from the higher-order terms. These first-order terms are completely determined from the free pion-nucleon phase shifts. (2) The important higher-order terms of the potential are further divided into two pieces: one associated with pion true absorption and dispersive effects, and the other associated with correlations. The correlation terms will be determined by a specific theoretical model. (3) The form of the absorption-dispersive terms is theoretically motivated from general considerations<sup>15</sup> of the pion-two-nucleon interaction. At the present time, however, the parameters characterizing the absorption-dispersive terms are not available from theory. To account for these effects, we introduce phenomenological isovector and isotensor absorption-dispersive parameters that are to be determined by the SCX and DCX data. The values of these parameters become the target for future theoretical investigations.

### A. General formulation

The theoretical framework we adopt is one that was successfully used in the resonance region to calculate pion-nucleus isoelastic scattering.<sup>15-17</sup> This approach is based upon two assumptions: (1) the pion-nucleus interaction is isospin invariant, and (2) the isobaric analog states together with the nuclear ground state are degenerate members of the same isotopic multiplet. Within this framework the general isospin operator dependence of the optical potential may be expressed as

$$\hat{U} = U_0 + (\boldsymbol{\phi} \cdot \mathbf{T})U_1 + (\boldsymbol{\phi} \cdot \mathbf{T})^2U_2, \quad (2.1)$$

where  $\boldsymbol{\phi}$  is the pion isospin operator and  $\mathbf{T}$  is the nuclear

isospin operator. Implicit in this definition is that  $\hat{U}$  projects the complete nuclear space onto a subspace that consists of the g.s., IAS, and DIAS. The nuclear density dependence and all of the pion-nucleus dynamics are described by the isoscalar, isovector, and isotensor potentials  $U_0$ ,  $U_1$ , and  $U_2$ . In principle, these potentials can be calculated microscopically by making a density expansion,

$$U_i = U_i^{(1)} + U_i^{(2)} + \dots, \quad (2.2)$$

where the superscript indicates the number of active nucleons, and  $i=0, 1$ , or  $2$ . The lowest-order contributions to the isoscalar and isovector potentials arise from the single-nucleon terms  $U_0^{(1)}$  and  $U_1^{(1)}$ , whereas the lowest-order contribution to the isotensor potential arises from the two-nucleon term  $U_2^{(2)}$ . [Of course, the two-nucleon (2N) term also contributes to the isoscalar and isovector potentials (i.e.,  $U_0^{(2)}$  and  $U_1^{(2)}$ ).]

A tacit assumption in the work of Refs. 15–17 is that the physics of pion-nucleus scattering is dominated by the first two terms of Eq. (2.2). In the (3,3) resonance region, this assumption is expected to be valid because the pion-nucleus interaction is surface dominated, occurring at densities on the order of 10% or less of the central density. At low energies, pion-nucleus reactions take place at higher densities. To account approximately for third- and higher-order terms in the series of Eq. (2.2), density-dependent renormalizations are incorporated into some of the terms.<sup>6</sup> It is plausible that this procedure is convergent because of the small value of the pion-nucleon cross section.

The calculation of various terms in the density expansion requires adopting a specific model for the underlying dynamics. There is, however, a general feature of the isospin-invariant formulation that is independent of the specific dynamical model assumed. Because we deal explicitly with nuclear states that are analogs of one another, predictions for  $U_0$ ,  $U_1$ , and  $U_2$  can be obtained conveniently from elastic matrix elements of  $U$  by using an inversion procedure.<sup>18</sup> Thus, the isospin-invariant formulation has the virtue that the full power of any theory of elastic scattering can be used to calculate SCX and DCX provided the isospin dependence of the theory is explicitly displayed.

Once an optical potential is defined, the procedure for obtaining the physical pion-nucleus transition amplitudes is to solve the appropriate one-body equation of motion, which we take as the Klein-Gordon equation. Formally, the pion optical potential is the proper self-energy of the pion Green's function and therefore enters the Klein-Gordon equation linearly. The general relation between the optical potential (2.1) and the resulting transition amplitudes is concisely displayed through the operator equation

$$\hat{F} = \hat{U} + \hat{U}\hat{G}\hat{F}, \quad (2.3)$$

where  $\hat{F}$  is the transition operator and  $G$  is the free pion-nucleus Klein-Gordon propagator, which is diagonal on the nuclear space. Thus, the only intermediate nuclear states that can occur explicitly in the  $\hat{U}\hat{G}\hat{F}$  term are the g.s., IAS, and DIAS. In analogy with Eq. (2.1), the iso-

spin operator dependence of the transition operator may be expressed as

$$\hat{F} = F_0 + (\boldsymbol{\phi} \cdot \mathbf{T})F_1 + (\boldsymbol{\phi} \cdot \mathbf{T})^2 F_2. \quad (2.4)$$

The SCX and DCX transition amplitudes can be obtained from this expression by taking the corresponding isospin matrix elements,<sup>18</sup>

$$\langle \pi^0, -T_0 + 1 | \hat{F} | \pi^+, -T_0 \rangle = \sqrt{T_0}(F_1 - T_0 F_2), \quad (2.5a)$$

$$\langle \pi^-, -T_0 + 2 | \hat{F} | \pi^+, -T_0 \rangle = \sqrt{T_0(2T_0 - 1)}F_2, \quad (2.5b)$$

where  $-T_0$  is the  $z$  component of the nuclear isospin  $T_0 = (N - Z)/2$ .

To calculate charge-exchange transition amplitudes from the isospin-channel potentials, we relate the  $F_i$ 's to the  $U_i$ 's by inserting the expressions for  $\hat{U}$  and  $\hat{F}$  given by Eqs. (2.1) and (2.4) into Eq. (2.3). This results in a set of coupled equations. (For completeness, this set of equations along with some details concerning the derivation are given in Appendix A.) Because the resulting set of equations for the  $F_i$ 's are coupled, we refer to this approach as the isospin-invariant coupled-channel (IICC) approach. Some general remarks concerning the content of charge-exchange calculations that result from the IICC approach and, in particular, the role of the isotensor potential follow.

Because the relations for  $F_0$ ,  $F_1$ , and  $F_2$  are coupled, they exhibit the property that, for a particular channel,  $F_i$  need not vanish when  $U_i = 0$ . An important example of this situation is for the case when  $U_2 = 0$ . In this case, the operator equation for the isotensor transition amplitude becomes [see Eq. (A4)]

$$F_2^{(\text{AR})} = U_1 G F_1 + (U_0 - 2U_1) G F_2^{(\text{AR})}. \quad (2.6)$$

We refer to this particular situation as the *analog route* to DCX; hence the label (AR). To explore the structure of the analog route further, consider the Born series expansion of Eq. (2.6),

$$F_2^{(\text{AR})} = U_1 G U_1 + U_1 G U_1 G U_0 + U_1 G U_0 G U_1 \\ + U_0 G U_1 G U_1 + \dots \quad (2.7)$$

The few terms explicitly displayed here are not meant as an approximation to the complete series, but are shown only to make the following point: the analog route to DCX involves, by definition, at least two actions of the isovector potential connected by at least one action of  $G$ . Recall that the propagator  $G$  is diagonal on the nuclear space and the potentials implicitly project onto the g.s., IAS, or DIAS. Therefore, DCX transitions via purely nonanalog intermediate states cannot occur in  $G$  and cannot be built out of iterations of  $U_0$  and  $U_1$ . To account for nonanalog intermediate states in DCX requires the addition of a  $U_2$ , and all such direct transition effects must be embedded within it. Examples of direct processes that contribute to  $U_2$  include correlated sequential scattering, pion true absorption and dispersion, pion-exchange-current interactions, and six-quark cluster effects. It is also clear that to prevent double counting, care must be taken when constructing models for  $U_2$  so that no analog route process is contained within it.

Before discussing our specific optical potential, we make one final comment concerning the numerical procedure we adopt to obtain IICC solutions for charge exchange. Instead of directly solving the coupled channel problem [as it appears in Eqs. (A4)], we project  $\hat{U}$  and  $\hat{F}$  onto channels of total (nuclear plus pion) isospin,

$$\hat{U} = \sum \Omega_I U_I \quad \text{and} \quad \hat{F} = \sum \Omega_I F_I, \quad (2.8)$$

where the  $\Omega$ 's are the projectors onto the total isospin channels  $I = T_0 + 1, T_0, T_0 - 1$ . The main advantage of going to channels of total isospin is that the resulting equations for  $F_I$  are diagonal in terms of the channel indices. From the definitions of the  $\Omega$ 's (which appear in Appendix A), we obtain the components  $U_I$  on this basis from the isoscalar, isovector, and isotensor components  $U_i$  ( $i=0,1,2$ ). This amounts to a unitary transformation from the one basis (indexed by  $i$ ) to another (indexed by  $I$ ). Our numerical procedure is to construct the  $U_I$ 's from model  $U_i$ 's, solve the diagonal equations for the  $F_I$ 's, and then construct the  $F_i$ 's by using the inverse transformation. This procedure is much easier to solve numerically than the original coupled equations. Physically, however, it is more natural to discuss the potential in terms of isoscalar, isovector, and isotensor components, and throughout this paper we shall continue to do so.

The above IICC procedure for calculating charge exchange cannot be used for elastic scattering because the Coulomb interaction is important and violates isospin invariance. We calculate elastic scattering by adding the Coulomb potential to the full optical potential given in Eq. (2.1) and by solving for the elastic amplitudes directly. This procedure does not allow intermediate IAS or DIAS charge exchange; however, we have determined that the influence of these coupled-channel effects is negligible for elastic scattering. The influence of the Coulomb interaction is also expected to be of some importance for low-energy SCX (unlike the situation at higher energies).<sup>19</sup> We show in Sec. V that, to a good approximation, Coulomb distortion effects can be ignored for 50-MeV SCX on light nuclei, but for nuclei with  $Z \geq 20$ , these effects can be significant.

### B. Specific optical potential

The specific form of the optical potential we adopt in this paper is the one used by Stricker, McManus, and Carr to describe low-energy elastic scattering.<sup>6</sup> If we explicitly separate the terms linear in the densities from the higher-order terms, the optical potential that results from the strong interactions can be written as<sup>16</sup>

$$\hat{U} = \nabla \cdot (\xi_p + \Delta\xi_p) \nabla - k^2 (\xi_s + \Delta\xi_s) - \frac{\nabla^2}{2} [(p_1 - 1)\xi_p + (p_2 - 1)\Delta\xi_p^{(2)}], \quad (2.9)$$

where  $\xi_s$  and  $\xi_p$  are, respectively, the  $s$ - and  $p$ -wave pion-nucleon contributions to the lowest-order potential;  $\Delta\xi_s$  and  $\Delta\xi_p$  refer, similarly, to the higher-order contributions. Each of these higher-order terms is further divided into two pieces,  $\Delta\xi = \Delta\xi^{(2)} + X$ , where  $\Delta\xi^{(2)}$  is associated with  $\pi$ -2N absorption and dispersion, and  $X$  is associated with

correlations. The quantity  $k$  is the pion's wave number in the pion-nucleus center of momentum, and the quantities  $p_1$  and  $p_2$  are kinematical factors that result from the frame transformation from the pion-nucleon ( $\pi$ -N) to the pion-nucleus ( $\pi$ -A) center of momentum. These are taken to be  $p_1 = (1 + \epsilon)/(1 + \epsilon/A)$  and  $p_2 = (1 + \epsilon/2)/(1 + \epsilon/A)$ , where  $\epsilon = (k^2 + m_\pi^2)^{1/2}/m_N$  and  $m_N$  ( $m_\pi$ ) is the nucleon's (pion's) mass (in units of  $\hbar = c = 1$ ).

The issue of higher-order contributions to the optical potential is an especially important one at low energies. In the absence of such modifications, the  $\pi$ -A interaction becomes very strong at low energy due to the presence of a phenomenon that has become known as the Kisslinger catastrophe.<sup>20</sup> Nuclear-medium modifications to the  $p$ -wave terms in the optical potential tend to regulate this singular behavior. Two types of effects that have been identified as significant in regulating the interaction are correlations<sup>21</sup> and self-consistent dispersive corrections.<sup>22</sup> Correlations in pion-nucleus scattering has received much attention, and we adopt specific theoretical models for these ( $X$ ) terms.

Many of the higher-order effects are model dependent and difficult to calculate. This includes pion true absorption and dispersion resulting from pion and nucleon interactions with the nuclear medium internal to the  $\pi$ -N scattering amplitude. Other such effects that may contribute significantly to the second-order optical potential include exchange currents<sup>23</sup> and six-quark cluster components to the 2N wave function.<sup>10</sup> To incorporate these relatively poorly known aspects of pion physics, we follow the usual procedure of introducing phenomenological parameters. We shall refer to these poorly known terms collectively as absorption-dispersive corrections ( $\Delta\xi^{(2)}$ ). Although we discuss these terms phenomenologically below, it is worth mentioning here that we find that the charge exchange data taken around 50 MeV can be described reasonably well with only two adjustable parameters.

Because we are interested in calculating charge exchange as well as elastic scattering, we intend to express the above potential in the form of Eq. (2.1). Thus, we will be paying particular attention to the isospin components of the various terms in Eq. (2.9). The terms that contribute to the first-order potential  $U^{(1)}$  are the so-called single-scattering terms (the  $\xi$ 's), and as mentioned in the previous section, they contribute to the isoscalar and isovector potentials. Their explicit isospin and density dependences can be written as

$$\xi_s = \xi_{s0} + (\phi \cdot \mathbf{T}) \xi_{s1} \quad \text{and} \quad \xi_p = \xi_{p0} + (\phi \cdot \mathbf{T}) \xi_{p1}, \quad (2.10a)$$

where for the isoscalar terms

$$\xi_{s0} = \lambda_{s0}^{(1)} \rho(r) \quad \text{and} \quad \xi_{p0} = \lambda_{p0}^{(1)} \rho(r), \quad (2.10b)$$

and for the isovector terms

$$\xi_{s1} = \lambda_{s1}^{(1)} \left[ \frac{\Delta\rho(r)}{2T_0} \right] \quad \text{and} \quad \xi_{p1} = \lambda_{p1}^{(1)} \left[ \frac{\Delta\rho(r)}{2T_0} \right]. \quad (2.10c)$$

The densities  $\rho$  and  $\Delta\rho$  are, respectively, the nuclear ground-state density and the excess neutron density. The  $\lambda^{(1)}$ 's are the first-order coupling coefficients (our notation is that without subscripts *all* the channels designated by

the omitted subscripts are implied). The  $\lambda^{(1)}$ 's are energy-dependent, complex quantities that we determine from the free  $\pi$ -N phase shifts of Arndt's analysis.<sup>24</sup> The specific relationships of the  $\lambda^{(1)}$ 's to the phase shifts are given in Appendix B. As in the MSU potential, the imaginary parts of the  $\lambda^{(1)}$ 's are Pauli blocked according to the nuclear matter prescription of Landau and McMillan.<sup>25</sup> We use a blocking factor of 0.3, which is associated with 50 MeV pions and a Fermi wave number  $k_f = 1.4 \text{ fm}^{-1}$ . With the phase shifts that we take, no adjustment of the parameters in the lowest-order potential is needed. Also in Appendix B the connections between our parameters and those of the MSU potential are given.

We next discuss the higher-order ( $\Delta\xi$ ) terms of Eq. (2.9). As mentioned above, the contributions to these terms are divided into absorption-dispersive parts ( $\Delta\xi^{(2)}$ ) and correlation parts ( $X$ ). Because these terms result from the pion interacting with two or more nucleons, they should contribute to the isoscalar, isovector, and isotensor potentials. The elastic scattering analysis of Ref. 6 is sensitive mostly to the isoscalar potential. To describe charge exchange, we find that corresponding isospin-dependent additions to the original potential are required by the data.

The higher-order  $s$ -wave term  $\Delta\xi_s$  is treated in the MSU potential as a second-order *isoscalar* term, i.e.,  $\Delta\xi_s \simeq \Delta\xi_{s0}$ . We write the absorption-dispersive part of this isoscalar term as,

$$\Delta\xi_{s0}^{(2)} = \lambda_{s0}^{(2)} \left[ \frac{\rho^2(r)}{\rho_0} \right], \quad (2.11)$$

where the complex parameter  $\lambda_{s0}^{(2)}$  describes isoscalar  $s$ -wave pion absorption on and dispersion from two nucleons. The constant density  $\rho_0 = 0.16 \text{ fm}^{-3}$  is introduced so that the first-order and second-order parameters ( $\lambda^{(1)}$  and  $\lambda^{(2)}$ ) have the same units. We take the strength of this parameter from Table IV, set C of the elastic scattering analysis of Stricker, Carr, and McManus.<sup>6</sup> This value corresponds to the strength (in MSU notation) of  $B_0 = (-0.02 + 0.14i) \text{ fm}^4$ .

The correlation part ( $X_{s0}$ ) of  $\Delta\xi_{s0}$  is taken to represent Pauli correlation effects only, and the specific form adopted by Ref. 6 results from nuclear matter considerations that actually render it linear in  $\rho$ .<sup>5</sup> We write this  $s$ -wave isoscalar correlation part as

$$X_{s0}(\rho) = -\frac{3k_f^2}{8\pi^2 p_1} k_F [(\lambda_{s0}^{(1)})^2 + \frac{1}{2}(\lambda_{s1}^{(1)})^2] \rho(r), \quad (2.12)$$

where  $k_f = 1.4 \text{ fm}^{-1}$  is taken to be a constant for all nuclei. By substantially increasing the isoscalar  $s$ -wave repulsion, this term plays an important role in the description of low-energy elastic scattering.

In addition to the isoscalar second-order  $s$ -wave term given above, we include a corresponding *isovector* second-order  $s$ -wave term,  $\Delta\xi_{s1}$ . For the absorption-dispersive part of this isovector term we write

$$\Delta\xi_{s1}^{(2)} = \lambda_{s1}^{(2)} \left[ \frac{\rho(r)}{\rho_0} \right] \left[ \frac{\Delta\rho(r)}{2T_0} \right], \quad (2.13)$$

where the complex parameter  $\lambda_{s1}^{(2)}$  describes isovector  $s$ -wave  $\pi$ -2N absorption and dispersion. The density depen-

dence is modeled after the considerations given in Ref. 15. By extending the arguments of Refs. 5 and 4, the isovector  $s$ -wave Pauli correlation term corresponding to the isoscalar form given in Eq. (2.12) can easily be obtained as

$$X_{s1}(\Delta\rho) = -\frac{3k_f^2}{8\pi^2 p_1} k_F [2\lambda_{s0}^{(1)}\lambda_{s1}^{(1)} - \frac{1}{2}(\lambda_{s1}^{(1)})^2] \frac{\Delta\rho(r)}{2T_0}. \quad (2.14)$$

Unlike the situation in the isoscalar  $s$ -wave channel, this term does not significantly increase the isovector  $s$ -wave repulsion.

In principle,  $s$ -wave absorption-dispersive effects and Pauli correlations will also contribute to an *isotensor*  $s$ -wave term,  $\Delta\xi_{s2}$ . These isotensor contributions may be expected to enter in a form analogous to their isoscalar and isovector counterparts. That is, for the isotensor  $s$ -wave absorption-dispersive term, we write

$$\Delta\xi_{s2}^{(2)} = \lambda_{s2}^{(2)} \left[ \frac{\Delta\rho(r)}{\rho_0} \right] \left[ \frac{\Delta\rho(r)}{T_0(2T_0-1)} \right], \quad (2.15)$$

where the density and isospin dependences are taken from the work of Ref. 15. In this expression, the  $T_0(2T_0-1)$  factor results from including *all* (nonanalog and analog) intermediate nuclear states. As for the isotensor Pauli correlation term ( $X_{s2}$ ), the model of Refs. 3–5 does not easily extend into the isotensor channel. For the purposes of this paper, we will not speculate on the form of this term, and we will take  $X_{s2} = 0$ .

In summary, the total contribution to the higher-order  $s$ -wave term appearing in Eq. (2.9) is

$$\Delta\xi_s = \Delta\xi_{s0} + (\boldsymbol{\phi} \cdot \mathbf{T}) \Delta\xi_{s1} + (\boldsymbol{\phi} \cdot \mathbf{T})^2 \Delta\xi_{s2}, \quad (2.16)$$

where each isospin component  $\Delta\xi_{si}$  ( $i=0,1,2$ ) is divided into a part associated with  $\pi$ -2N absorption-dispersive effects and a part associated with correlations, i.e.,  $\Delta\xi_{si} = \Delta\xi_{si}^{(2)} + X_{si}$ . The density and isospin dependences of these separate contributions are given in Eqs. (2.11)–(2.15). In the present model,  $s$ -wave correlations are assumed to result from Pauli effects only, and these terms are determined by a theoretical calculation. The remaining unknown absorption-dispersive terms are characterized by three complex numbers ( $\lambda_{si}^{(2)}$ ) that govern the strengths of their isospin components. The isoscalar parameter  $\lambda_{s0}^{(2)}$  is taken from the elastic analysis of Ref. 6. The isovector and isotensor parameters ( $\lambda_{s1}^{(2)}$  and  $\lambda_{s2}^{(2)}$ ) are not known; however, we find that these pieces are not required by the data at 50 MeV.

Next we consider the higher-order  $p$ -wave term,  $\Delta\xi_p$ . For this term, the contributions included in the MSU potential are also divided into parts arising from absorption-dispersive effects and those arising from correlations. In analogy with the treatment of the  $s$ -wave term, the  $p$ -wave absorption-dispersive part is considered to be a second-order isoscalar term of the form

$$\Delta\xi_{p0}^{(2)} = \lambda_{p0}^{(2)} \left[ \frac{\rho^2(r)}{\rho_0} \right]. \quad (2.17)$$

We determine the isoscalar parameter  $\lambda_{p0}^{(2)}$  from the parameter  $C_0 = (0.36 + 0.51i) \text{ fm}^6$ , which comes from Table

IV, set C of Stricker, Carr, and McManus.<sup>6</sup>

As in the case for the  $s$ -wave terms, we also include corresponding isovector and isotensor second-order  $p$ -wave absorption-dispersive terms,

$$\Delta\xi_{p1}^{(2)} = \lambda_{p1}^{(2)} \left[ \frac{\rho(r)}{\rho_0} \right] \left[ \frac{\Delta\rho(r)}{2T_0} \right] \quad (2.18)$$

and

$$\Delta\xi_{p2}^{(2)} = \lambda_{p2}^{(2)} \left[ \frac{\Delta\rho(r)}{\rho_0} \right] \left[ \frac{\Delta\rho(r)}{T_0(2T_0-1)} \right], \quad (2.19)$$

respectively. The density and isospin dependences of these terms are modeled (as for  $s$  waves) after the considerations of Ref. 15. The total contribution of the  $p$ -wave absorption-dispersive terms is then

$$\Delta\xi_p^{(2)} = \Delta\xi_{p0}^{(2)} + (\boldsymbol{\phi} \cdot \mathbf{T}) \Delta\xi_{p1}^{(2)} + (\boldsymbol{\phi} \cdot \mathbf{T})^2 \Delta\xi_{p2}^{(2)}. \quad (2.20)$$

Unlike the situation for the  $s$ -wave absorption-dispersive terms, we do find a need for an imaginary isovector  $p$ -wave term ( $\text{Im}\lambda_{p1}^{(2)}$ ) and a real isotensor  $p$ -wave term ( $\text{Re}\lambda_{p2}^{(2)}$ ) in order to describe the SCX and DCX data near 50 MeV. The values for these coefficients are given and discussed later, in Sec. IV.

We close this section by mentioning the isospin components of the  $p$ -wave correlation effects ( $X_p$ ). As for the corresponding  $s$ -wave terms, we take the  $p$ -wave correlation effects from a theoretical calculation. These effects are incorporated in the MSU potential as a density-dependent renormalization of the lowest-order potential. The renormalization factor takes the familiar form of the Lorentz-Lorenz Ericson-Ericson effect.<sup>3</sup> Because there has been some controversy about this particular formulation of  $p$ -wave correlations, and because we find the isospin components of this term significantly affect our charge-exchange calculations, we devote the next section to a discussion of low-energy  $p$ -wave correlations.

### III. CORRELATIONS IN LOW-ENERGY PION SCATTERING

Our objective in this section is to present the isospin decomposition of the  $p$ -wave correlation term  $X_p$ . We approach this objective in two steps. First, we examine the standard Lorentz-Lorenz Ericson-Ericson term as incorporated in the MSU potential<sup>3</sup> and as discussed by Friedman and Gal.<sup>26</sup> Next, we make contact with microscopic theory to calculate the corresponding isoscalar, isovector, and isotensor correlation strength parameters based on a specific model.

Nuclear correlations and their effects on  $\pi$ - $A$  scattering have had a long and somewhat confusing history. The importance of short-range repulsive nucleon-nucleon correlations to  $\pi$ - $A$  elastic scattering and pionic atoms was demonstrated long ago and has become known as the Lorentz-Lorenz Ericson-Ericson (LLEE) effect.<sup>3</sup> Subsequent calculations by Eisenberg, Hufner, and Moniz<sup>7</sup> indicated that these correlation effects could disappear when finite range  $\pi$ -N form factors are taken into account, but Barshay, Brown, and Rho<sup>8</sup> argued that the  $\pi$ -N form factors of Ref. 7 were too severe. Later work indicated that

rho-meson exchange<sup>27</sup> and Pauli correlations<sup>28</sup> should be considered along with the original short-range LLEE effect. Careful attempts to find correlation effects phenomenologically from  $\pi$ - $A$  elastic scattering and pionic atoms were inconclusive;<sup>9</sup> the studies in this section lay the foundation for looking in Sec. IV at the evidence for correlations in  $\pi$ - $A$  charge-exchange scattering.

In this paper we associate the term "correlations" with the combined LLEE,  $p$ -wave Pauli, and rho-meson effects and lump them together into a separate term of the optical potential. In order that this term not be confused with the LLEE effect alone, we refer to this term as the *extended* Lorentz-Lorenz (EL) effect.

Let us begin with the standard LLEE form as used in the MSU potential. We expand in powers of  $\Delta\rho$  to obtain the appropriate isospin components necessary for our charge-exchange calculations. In this formulation of the optical potential [Eq. (2.9)], the EL effect appears as a higher-order term,

$$X_p = -\frac{\alpha}{3} (\xi_p)^2 \left[ 1 + \frac{\alpha}{3} \xi_p \right]^{-1}, \quad (3.1)$$

where  $\alpha$  is the dimensionless EL correlation parameter. This term is added to the  $p$ -wave absorption-dispersive term in Eq. (2.20) to give the total higher-order  $p$ -wave contribution to the optical potential. To recover the form of the  $p$ -wave potential used in Ref. 3 the single-scattering term must be added to the  $X_p$  term given here.

From the isospin dependence of the first-order  $p$ -wave term ( $\xi_p$ ) given in Eq. (2.10), we see that in addition to an extended Lorentz-Lorenz isoscalar (ELIS) term in Eq. (3.1), there are implied isovector (ELIV) and isotensor (ELIT) correlation terms. In this simple model, the value of the EL correlation parameter  $\alpha$  given by any set of elastic scattering parameters from Ref. 6 completely specifies these isospin dependent correlation terms. The more microscopic approach to  $p$ -wave correlation effects discussed below indicates that the different correlation parameters for the various isospin components are approximately equal to a model used in Ref. 6.

To display the implied isospin dependence of the EL term explicitly, we rewrite Eq. (3.1) in the form

$$X_p = X_{p0} + (\boldsymbol{\phi} \cdot \mathbf{T}) X_{p1} + (\boldsymbol{\phi} \cdot \mathbf{T})^2 X_{p2}, \quad (3.2)$$

where the ELIS, ELIV, and ELIT terms can be obtained by taking the appropriate linear combinations of elastic matrix elements as mentioned in Sec. II. A brief outline of the algebraic manipulations along with the exact results is given in Appendix C. In this paper, we use the relatively simple form of the isospin components of  $X_p$ , which are obtained by neglecting terms of order  $(\Delta\rho)^3$  and higher. The results are

$$X_{p0} = L_0(\rho) \rho^2, \quad (3.3a)$$

$$X_{p1} = L_1(\rho) \left[ \frac{\rho \Delta\rho}{2T_0} \right], \quad (3.3b)$$

$$X_{p2} = L_2(\rho) \left[ \frac{\Delta\rho}{2T_0} \right]^2, \quad (3.3c)$$

where

$$\begin{aligned} L_0(\rho) &= -\frac{\alpha_0}{3} L(\lambda_{p0}^{(1)})^2, \\ L_1(\rho) &= -\frac{2\alpha_1}{3} L^2 \left[ 1 + \frac{\alpha}{6} \lambda_{p0}^{(1)} \lambda_{p1}^{(1)} \right] (\lambda_{p0}^{(1)} \lambda_{p1}^{(1)}), \\ L_2(\rho) &= -\frac{\alpha_2}{3} L^3 (\lambda_{p1}^{(1)})^2, \end{aligned} \quad (3.3d)$$

in terms of the complete isoscalar EL term  $L^{-1} = [1 + (\alpha_0/3)\lambda_{p0}^{(1)}]$ . We have added subscripts to the EL correlation parameters so that we may distinguish them from each other. We note that these expressions include all powers of  $\rho$ , and because of the smallness of  $\Delta\rho$ , they should be excellent approximations to the exact results. A similar (but not identical) isospin decomposition of the LEE factor has been obtained by Friedman and Gal.<sup>26</sup>

To choose values for  $\alpha_0$ ,  $\alpha_1$ , and  $\alpha_2$  we make contact with a microscopic calculation which explicitly includes short-range correlations, Pauli correlations, and rho-meson exchange. This microscopic approach follows the work of Ref. 15, where the second-order diagrams shown in Fig. 1 are evaluated within a fixed-source field theory for 50-MeV  $p$ -wave  $\pi$ -N amplitudes. The following ingredients are included in this calculation: Short-range correlations are described with a cutoff radial distribution function that prevents the relative N-N coordinate from being less than 0.5 fm. The nuclear density matrices are treated in a surface-corrected local-density approximation, which incorporates the exponential falloff of the nuclear wave functions. Intermediate  $\pi$ - $A$  interactions are accounted for by using a renormalized local-density form for the intermediate pion propagator. Finite-range meson-nucleon form factors of the form  $v(k) = (1 + k^2/\Lambda^2)^{-1}$  are used, and for the rho-meson couplings we assume

$$f_{\rho N\Delta}/f_{\pi N\Delta} = f_{\rho NN}/f_{\pi NN} = \sqrt{2}m_\rho/m_\pi$$

(Ref. 29). Finally, kinematic approximations made in Ref. 15 that were applicable only at resonance energies are corrected for low-energies.

To obtain the EL correlation parameters from the microscopic approach of Ref. 15, we equate the corresponding isospin components from Eq. (3.2) of this paper to those of Eq. (5.35) of Ref. 15. By so doing, we find the following results:

$$X_{p0}^{(2)} = \left[ \frac{\rho^2}{\rho_0} \right] \lambda_0 + \left[ \frac{\Delta\rho^2}{\rho_0} \right] \left[ \lambda_3 - \left[ \frac{1}{2T_0 - 1} \right] \lambda_2 \right], \quad (3.4a)$$

$$X_{p1}^{(2)} = \left[ \frac{\rho\Delta\rho}{2T_0\rho_0} \right] \lambda_1 + \left[ \frac{\Delta\rho^2}{2T_0(2T_0 - 1)\rho_0} \right] \lambda_2, \quad (3.4b)$$

$$X_{p2}^{(2)} = \left[ \frac{\Delta\rho^2}{\rho_0} \right] \left\{ \left[ \frac{1}{T_0(2T_0 - 1)} \right] \lambda_2 + \left[ \frac{1}{T_0^2} \right] \lambda_4 \right\}, \quad (3.4c)$$

where the  $\lambda$ 's appearing here are the results of the microscopic second-order calculations associated with the dia-

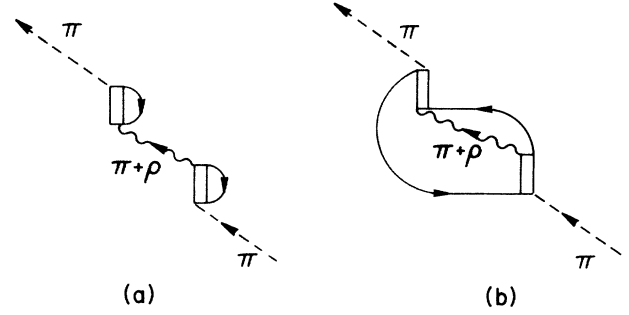


FIG. 1. Two-nucleon processes evaluated to determine the EL correlation factors. Pauli correlations enter through (b). Short range repulsive correlations keep nucleons apart in (a) and (b).

grams in Fig. 1. Because these calculations are for  $\pi$ -2N processes, the  $X_p$ 's appearing in Eqs. (3.4) have the appropriate superscript. These second-order  $X_p$ 's are found by using the  $\rho=0$  values of the  $L_i$ 's in Eqs. (3.3d), i.e.,  $L_0 = -\alpha_0(\lambda_{p0}^{(1)})^2/3$ ,  $L_1 = -2\alpha_1(\lambda_{p0}^{(1)}\lambda_{p1}^{(1)})/3$ , and  $L_2 = -\alpha_2(\lambda_{p1}^{(1)})^2/3$ . Now, by using the second-order  $X_p$ 's in Eqs. (3.3a)–(3.3c) that result from these values of the  $L_i$ 's, we can use Eqs. (3.4) to obtain expressions for the  $\alpha$ 's in terms of the calculated  $\lambda$ 's. The resulting expressions are

$$\alpha_0 = -\frac{3}{\rho_0(\lambda_{p0}^{(1)})^2} \left\{ \lambda_0 + \left[ \frac{N-Z}{A} \right]^2 \left[ \lambda_3 - \left[ \frac{1}{2T_0 - 1} \right] \lambda_2 \right] \right\}, \quad (3.5a)$$

$$\alpha_1 = -\frac{3}{2\rho_0(\lambda_{p0}^{(1)}\lambda_{p1}^{(1)})} \left[ \lambda_1 + \left[ \frac{N-Z}{A} \right] \left[ \frac{1}{2T_0 - 1} \right] \lambda_2 \right], \quad (3.5b)$$

$$\alpha_2 = -\frac{12}{\rho_0(\lambda_{p1}^{(1)})^2} \left[ \left[ \frac{T_0}{2T_0 - 1} \right] \lambda_2 + \lambda_4 \right]. \quad (3.5c)$$

The  $(N-Z)/A$  factors in the expressions for  $\alpha_0$  and  $\alpha_1$  result from  $\Delta\rho/\rho$  factors in the model, and numerically the contributions from the terms including these  $(N-Z)/A$  factors turn out to be insignificant. The  $T_0/(2T_0 - 1)$  factor in the expression for  $\alpha_2$  results (in the model of Ref. 15) from including *all* intermediate nuclear states (analog and nonanalog), and the  $\lambda_4$  term subtracts the analog route component so that no double counting takes place.

The theory of Ref. 15 yields complex values for the  $\lambda$ 's, and thus, via Eqs. (3.5), gives rise to complex  $\alpha$  parameters. The imaginary parts arise mostly from the Pauli exchange diagram [Fig. 1(b)]. In the following discussion of our calculations for the  $\alpha$ 's, we omit the imaginary parts in order to stay as close as possible to the MSU procedure for Pauli blocking. In the MSU approach the imaginary parts of the single-scattering terms are calculated according to the prescription of Landau and McMillan.

In Table I we show our microscopic results for the EL

TABLE I. Effects of short-range correlations, Pauli correlations, and rho-meson exchange at 50 MeV on the calculation of the EL correlation parameters  $\alpha_0$ ,  $\alpha_1$ , and  $\alpha_2$ . The top three rows are for pi-meson exchange only. The bottom three rows include both the pi and rho meson.

$\Lambda$ (fm $^{-1}$ )	$\alpha_0$		$\alpha_1$		$\alpha_2$	
	1(a)	1(a) + 1(b)	1(a)	1(a) + 1(b)	1(a)	1(a) + 1(b)
( $\pi$ )20	1.09	1.34	1.06	0.99	1.01	1.21
( $\pi$ )10	0.79	1.22	0.78	0.89	0.69	1.05
( $\pi$ )6	0.46	1.09	0.45	0.77	0.32	0.86
( $\pi$ + $\rho$ )20	3.05	2.14	2.98	1.68	3.20	2.38
( $\pi$ + $\rho$ )10	2.60	1.99	2.55	1.56	2.72	2.18
( $\pi$ + $\rho$ )6	1.61	1.69	1.58	1.29	1.61	1.71

correlation parameters obtained through the use of Eqs. (3.5). The first-order quantities (the  $\lambda^{(1)}$ 's) in this calculation are determined from the 50-MeV  $\pi$ -N phase shifts,<sup>24</sup> and the constant central density is taken as  $\rho_0=0.16$  fm $^{-3}$ . The columns of this table labeled 1(a) result from using the direct diagram only, as depicted in Fig. 1(a). The columns labeled 1(a) + 1(b) result from calculating both the direct and exchange diagrams, Figs. 1(a) and 1(b). Short-range correlations between the two nucleons are included in all the results given here. The top three rows result from evaluating intermediate pion exchange only, with the  $\pi$ -N form factor range set to values of  $\Lambda_\pi=20$ , 10, and 6 fm $^{-1}$ . By reading down the top three rows of the columns labeled 1(a), we see that the short-range correlation contribution to the  $\alpha$ 's falls off as  $\Lambda_\pi$  decreases. By reading down the columns labeled 1(a) + 1(b), we see, however, that the Pauli effect tends to compensate and leaves the magnitudes of the  $\alpha$ 's rather insensitive to the  $\pi$ -N range.

In the bottom three rows of Table I, we give our results of including both pi- and rho-meson exchange with  $\Lambda_\pi=\Lambda_\rho=20$ , 10, and 6 fm $^{-1}$ . We see that as  $\Lambda_\rho$  increases, the  $\alpha$ 's resulting from the direct diagram 1(a) become large. By including the exchange diagram 1(b), the corresponding  $\alpha$ 's tend to be reduced in size (as contrasted to the pion-exchange-only results which show the Pauli effect to increase the values of the  $\alpha$ 's). Having an  $\alpha_0$  close to unity is important. It is pointed out in Ref. 30 that if dispersive effects contained in  $C_0$  of the MSU potential are included with  $\alpha_0$ , giving  $\alpha'_0$ , then  $\alpha_0 > \alpha'_0 \approx 1$ . One can understand the transparency of the nucleus to pions at low energy in terms of  $\alpha'_0$  being close to unity:  $\alpha'_0=1$  is just the value needed to cancel the double-scattering term of the multiple scattering expansion.<sup>21</sup> As we will see, experiment indicates that  $\pi$ -A SCX is also similar to  $\pi$ -N SCX, and thus we might expect a similar role for correlations plus dispersion in the isovector channel.

For the realistic values<sup>31</sup>  $\Lambda_\pi \approx \Lambda_\rho \approx 6.0$  fm $^{-1}$ , our complete calculation, including rho-meson exchange, short-range, and Pauli correlations [sixth row results labeled 1(a) + 1(b)], we find  $\alpha_0 \approx 1.7$ ,  $\alpha_1 \approx 1.3$ , and  $\alpha_2 \approx 1.7$ . These values are comparable to each other and close to those used in the MSU potential. We also found these values of the  $\alpha$ 's to be relatively insensitive to other variations in our calculations. However, if the rho-meson and inter-

mediate  $\pi$ -A interactions are omitted, we find that the value of  $\alpha_2$  can be significantly altered in magnitude and sign, depending on the exact treatment of the short-range correlations and nuclear densities.

From Eqs. (3.3) we note that the resulting  $X_p$ 's will be negative definite. This implies that both the  $X_{p0}$  and  $X_{p1}$  terms, when added to the first-order potential, will respectively decrease the isoscalar and isovector  $p$ -wave attraction. There is no first-order isotensor potential for the  $X_{p2}$  term to decrease, but, as shown below, the  $X_{p2}$  term destructively interferes with the analog route amplitude. The numerical influence of the  $X_{p0}$  term on elastic scattering has been thoroughly investigated (see Ref. 6). In the next section, we numerically demonstrate that the corresponding influences of the  $X_{p1}$  and  $X_{p2}$  terms on SCX and DCX are significant. This suggests that these effects must be included in all serious calculations of low-energy SCX and DCX.

#### IV. NUMERICAL RESULTS OF THE ISOSPIN-INVARIANT MODEL

In this section we display and discuss calculations near the 50-MeV region that result from the IICC formulation and the optical potential specified in the previous sections. The main points observed from these calculations are the following: (1) Elastic scattering is well described, and the ELIV and ELIT terms do not significantly affect these calculations. (2) The ELIV term significantly affects the SCX and analog route DCX calculations. (3) The ELIT term does not significantly affect SCX, but for forward direction DCX it causes a destructive interference with the analog route. (4) Comparison to SCX data tends to support the ELIV effects, whereas the DCX data indicates the need for some additional process to interfere *constructively* with the analog route.

Before we discuss our results, we briefly review and specify the parameters that characterize the potential. We have expressed the MSU form of the low-energy optical potential given by Eq. (2.9) in terms of its isospin components

$$\hat{U} = U_0 + (\boldsymbol{\phi} \cdot \mathbf{T})U_1 + (\boldsymbol{\phi} \cdot \mathbf{T})^2 U_2, \quad (4.1)$$

where for each component ( $i=0,1,2$ )

$$U_i = \nabla \cdot (\xi_{pi} + \Delta \xi_{pi}^{(2)} + X_{pi}) \nabla - k^2 (\xi_{si} + \Delta \xi_{si}^{(2)} + X_{si}) - \frac{\nabla^2}{2} [(p_1 - 1)\xi_{pi} + (p_2 - 1)\Delta \xi_{pi}^{(2)}]. \quad (4.2)$$

The  $\xi_{si}$  and  $\xi_{pi}$  terms in this expression are the first-order (or single-scattering) terms and contribute to the isoscalar ( $i=0$ ) and isovector ( $i=1$ ) potentials only, i.e.,  $\xi_{s2} \equiv \xi_{p2} \equiv 0$ . The quantities that specify the strengths of these terms are designated  $\lambda_{si}^{(1)}$  and  $\lambda_{pi}^{(1)}$ , and are theoretically determined as discussed in Sec. II B.

The  $X_{si}$  and  $X_{pi}$  terms in Eq. (4.2) are the correlation terms, and are also theoretically determined. The  $s$ -wave  $X_{si}$ 's are calculated in terms of the  $\lambda_{si}^{(1)}$ 's and the Fermi wave number ( $k_f$ ) according to Eqs. (2.12) and (2.14). The  $p$ -wave  $X_{pi}$ 's are fixed by Eqs. (3.3) in terms of the  $\lambda_{pi}^{(1)}$ 's and the EL correlation parameters  $\alpha_0$ ,  $\alpha_1$ , and  $\alpha_2$ . We take, for simplicity,  $\alpha_0 = \alpha_1 = \alpha_2 = 1.6$ , which corresponds roughly to our  $\Lambda_\pi = \Lambda_\rho = 6 \text{ fm}^{-1}$  calculations in Table I. This value of  $\alpha$  has also been used by Stricker, Carr, and McManus (Table IV, set C) in the analysis of 50 MeV elastic scattering.<sup>6</sup>

The  $\Delta \xi_{si}^{(2)}$  and  $\Delta \xi_{pi}^{(2)}$  terms in Eq. (4.2) characterize the absorption-dispersive effects, and are defined by Eqs. (2.11)–(2.19). The strengths of these terms are governed by the  $\lambda_{si}^{(2)}$  and  $\lambda_{pi}^{(2)}$  parameters. As mentioned in Sec. II B, we take the isoscalar parameters ( $\lambda_{s0}^{(2)}$  and  $\lambda_{p0}^{(2)}$ ) from the 50-MeV elastic scattering analysis of Stricker, Carr, and McManus.<sup>6</sup> Although there is some uncertainty in these values of the isoscalar parameters (depending, for example, on the procedure for extrapolating from zero energy), we feel that this choice is representative. The remaining isovector and isotensor absorption-dispersive parameters are relatively unknown at this time; thus, unless stated otherwise, we set them to zero.

For ease of future reference, we list the values of all the 50-MeV optical-potential parameters in Table II. Unless

stated otherwise, we use the  $N/Z$  scaling model for the nuclear densities, where  $\rho_p$  is determined from electron scattering<sup>32</sup> and  $\rho_n = (N/Z)\rho_p$ . The point proton-density parameters we use in this model are corrected for the finite size of the proton and are given in Table III.

To perform ICC calculations, we have extended the coordinate-space computer code PIESDEX (Ref. 16) so that the full density-dependence of the ELIS, ELIV, and ELIT terms can be incorporated. With PIESDEX, the Klein-Gordon equation is solved numerically for scattering amplitudes on channels of total isospin, and the appropriate linear combinations of these total isospin amplitudes are used to obtain the charge-exchange amplitudes. For elastic scattering, the Coulomb potential is added to the full optical potential, and the elastic amplitudes are calculated directly (without going to the total isospin representation). The influence of the Coulomb interaction is not included in the ICC results for charge exchange shown in this section, but it is included in the DWBA results in Sec. V.

To demonstrate that our choice of parameters provides a reasonable qualitative description of elastic scattering, we compare some of our results to 50 MeV  $\pi^+$  data in Fig. 2. The solid curves result from including the ELIV term [Eq. (3.3b)], whereas the short-dashed curves result from omitting it. For the  $T_0 = 0$  nuclei there is, of course, no difference. But even for the  $T_0 \neq 0$  nuclei, the influence of the ELIV term is relatively minor: it slightly deepens the cross-section minima for these nuclei. The effect of the ELIT term [Eq. (3.3c)] upon elastic scattering is insignificant and the elastic scattering calculations that result from including both the ELIV and ELIT terms cannot be distinguished from the solid curves. Although these calculations agree reasonably well with the data, the agreement can easily be improved by slightly adjusting the isoscalar absorption-dispersive parameters.<sup>34</sup>

For the corresponding 50-MeV SCX calculations, the

TABLE II. Optical potential parameters for 50 MeV. The  $\lambda$ 's depend upon  $A$  through the frame transformation factors  $p_1$  and  $p_2$ , but the variation is at most 1%. The values given here are for  $^{14}\text{C}$ . Also, the listed  $\text{Im}(\lambda^{(1)})$ 's are multiplied by a Pauli blocking factor of 0.3.

Parameter	Origin	Values
First-order isoscalar	$\pi$ -N phase shifts Ref. 24	$\lambda_{s0}^{(1)} = (-2.39 + 0.22i) \text{ fm}^3$ ; $\lambda_{p0}^{(1)} = (8.40 + 0.32i) \text{ fm}^3$
First-order isovector	$\pi$ -N phase shifts Ref. 24	$\lambda_{s1}^{(1)} = (-9.12 + 0.15i) \text{ fm}^3$ ; $\lambda_{p1}^{(1)} = (10.91 + 0.30i) \text{ fm}^3$
Second-order isoscalar	Pionic atoms and elastic scattering analysis, Ref. 6	$\lambda_{s0}^{(2)} = (-0.11 + 0.74i) \text{ fm}^3$ ; $\lambda_{p0}^{(2)} = (0.67 + 1.09i) \text{ fm}^3$
Second-order isovector	Phenomenological analysis of SCX	$\lambda_{s1}^{(2)} = \lambda_{p1}^{(2)} = \text{zero}^a$
Second-order isotensor	Phenomenological analysis of DCX	$\lambda_{s2}^{(2)} = \lambda_{p2}^{(2)} = \text{zero}^a$
EL correlation strength	Sec. III and Ref. 6	$\alpha_i = \alpha = 1.6$
Fermi wave number used in $s$ -wave correlation term	Ref. 6	$k_f = 1.4 \text{ fm}^{-1}$

<sup>a</sup>Except for Figs. 5 and 11, where the effects of  $\text{Im}\lambda_{p1}^{(2)} = -1.0 \text{ fm}^3$  on SCX are shown, and for Fig. 6, where the effects of  $\text{Re}\lambda_{p2}^{(2)} = +1.7 \text{ fm}^3$  on DCX are shown.

TABLE III. Point proton-density shapes and parameters.

	$\rho = \rho_0 [1 + w(r/a)^2] \exp(-r^2/a^2)$				
	$^{14}\text{C}$	$^{15}\text{N}$	$^{16}\text{O}$	$^{18}\text{O}$	
$a$ (fm)	1.66	1.69	1.75	1.80	
$w$	1.80	1.67	1.54	1.79	
	$\rho = \rho_0 [1 + w(r/c)^2] \{1 + \exp[(r-c)/a]\}^{-1}$				
	$^{39}\text{K}$	$^{40}\text{Ca}$	$^{48}\text{Ca}$	$^{90}\text{Zr}$	$^{208}\text{Pb}$
$a$ (fm)	0.586	0.520	0.525	0.528	0.505
$c$ (fm)	3.74	3.52	3.77	4.86	6.62
$w$	-0.201	0.0	-0.03	0.0	0.0

influence of the ELIV term is quite pronounced because of the near cancellation between the  $s$ - and  $p$ -wave first-order terms in the forward direction. We display some of these results in Fig. 3. The short-dashed curves result from omitting the ELIV and ELIT terms. This amounts to using only the lowest-order isovector potential to calculate SCX. The long-dashed curves result from including the ELIV terms, and the solid curves result from including both the ELIV and ELIT terms. From these results we see that the inclusion of the ELIV term has the effect of systematically decreasing and shifting the calculated cross sections. The most dramatic effect can be seen in the forward direction of the lighter nuclei, where the ELIV effect changes the maxima at  $\theta = 0^\circ$  into minima. We also note from Fig. 3 that the effect of the ELIT term upon SCX is minuscule: it causes an additional small

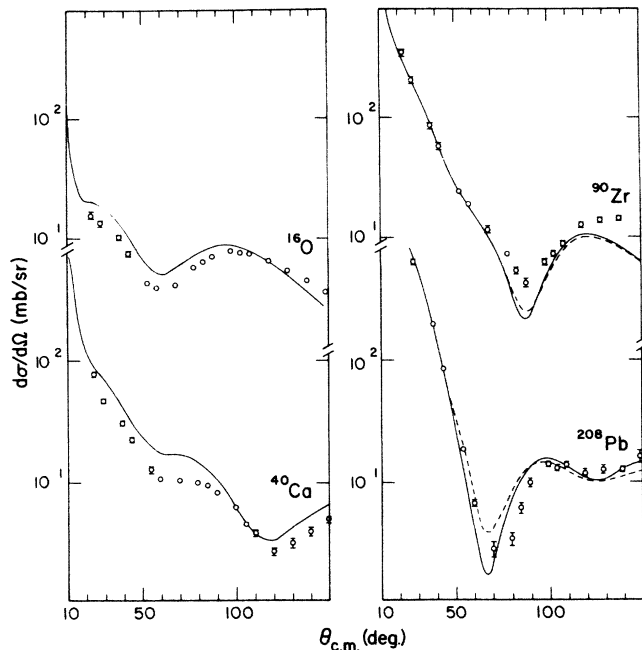


FIG. 2. Comparison of IICC calculations with the data (Ref. 33) for 50-MeV  $\pi^+$  elastic scattering on several nuclei. The solid curves include the ELIV term and the dashed curves do not.

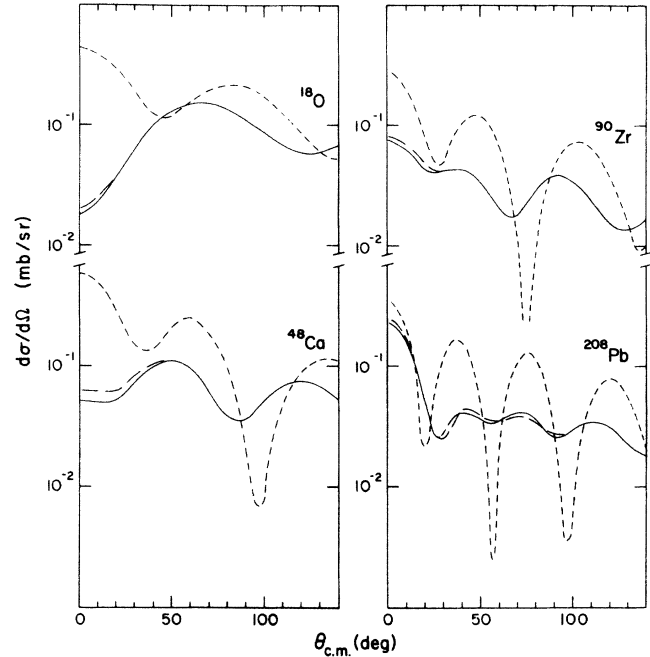


FIG. 3. IICC calculations of 50-MeV  $\pi^+$  SCX to the IAS on several nuclei. The solid curves include both ELIV and ELIT terms, the long-dashed curves have only the ELIV term, and the short-dashed curves have neither.

reduction beyond that of the ELIV effect in the forward direction.

In Fig. 4, we show the corresponding DCX calculations. As in Fig. 3, the solid, long-dashed, and short-dashed curves correspond to including both the ELIV and ELIT terms, only the ELIV term, and neither the ELIV nor ELIT terms, respectively. Although the ELIT term does influence the calculations, we see that the largest effect upon DCX apparently results from including the ELIV term (comparing the short-dashed to the long-dashed curves). We further note that both of the dashed curves result from analog route calculations of DCX, i.e.,  $U_2 = 0$ . The difference between them, of course, results from the different models of  $U_1$ . It is interesting to observe that the inclusion of the ELIV systematically lowers the SCX cross sections, whereas for DCX it increases the cross section for the lightest nucleus and decreases the cross sections for the others.

To see if there is any experimental evidence in support of the isovector and isotensor correlative effects demonstrated above, we now compare our calculations to some of the recent charge-exchange data taken for incident pion energies near 50 MeV. In Fig. 5, we compare our SCX calculations to some of the  $(\pi^+, \pi^0)$  IAS data. Because the ELIT term has a negligible effect on SCX calculations, we have omitted it from the potential used to obtain the curves shown in this figure. The solid curves result from including the ELIV term only. (These results corresponding to those of Fig. 3 shown by the long-dashed curves.)

As mentioned above in the discussion of Fig. 3, the in-

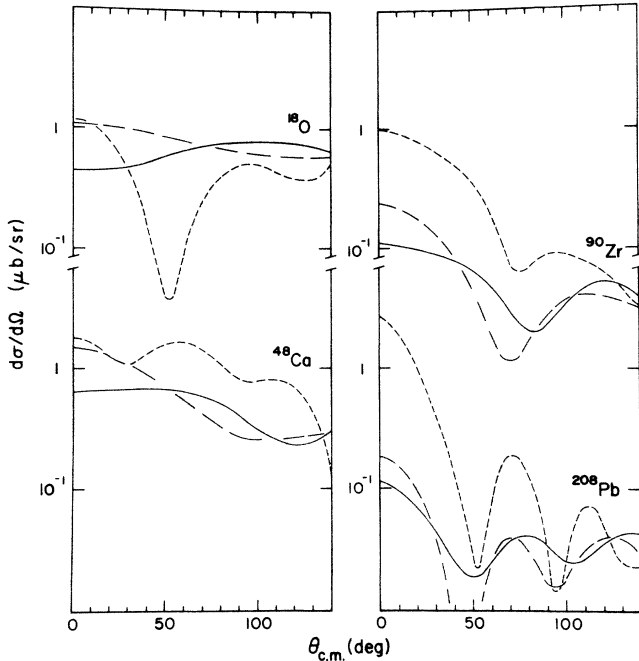


FIG. 4. IICC calculations of 50-MeV  $\pi^+$  DCX to the DIAS on several nuclei. The solid curves include both the ELIV and ELIT terms, the long-dashed curves have only the ELIV, and the short-dashed curves have neither.

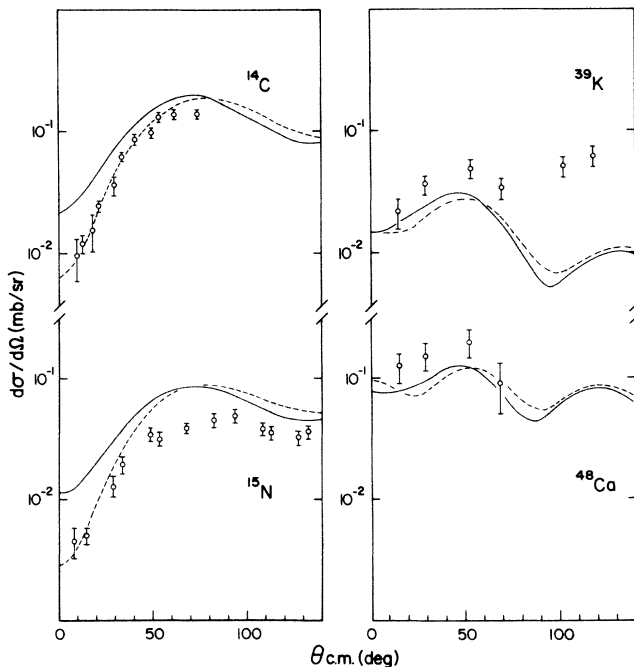


FIG. 5. Comparison of 50-MeV  $\pi^+$  SCX data (Refs. 12, 1, and 11) to IICC calculations for several nuclei. The solid curves include the ELIV term with no ELIT term and the dashed curves contain in addition an imaginary second-order  $p$ -wave isovector term [ $\lambda_{p1}^{(2)} = (0 - 1.0i) \text{ fm}^{-3}$ ].

clusion of the ELIV term produces forward-angle minima in the calculations. By comparing the data to the solid curves in Fig. 5, we see that within our calculational framework the data tend to support the need for the ELIV term. In fact, the data on  $^{14}\text{C}$  and  $^{15}\text{N}$  show much deeper forward minima than those given by the solid curves, whereas the forward-angle calculated cross sections for  $^{39}\text{K}$  and  $^{48}\text{Ca}$  are in reasonable agreement with the data. In an attempt to phenomenologically alleviate this discrepancy, we explored the influence of the  $s$ -wave and  $p$ -wave second-order isovector absorption-dispersive terms [given in Eqs. (2.13) and (2.18)] by arbitrarily setting the real and imaginary parts of the strength parameters  $\lambda_{s1}^{(2)}$  and  $\lambda_{p1}^{(2)}$  to values of  $\pm 1.0 \text{ fm}^3$ . We found the imaginary part of the  $p$ -wave term to have the desired effect on the SCX cross sections. The dashed curves in Fig. 5 show the results when an isovector  $p$ -wave absorption of strength  $\text{Im}\{\lambda_{p1}^{(2)}\} = -1.0 \text{ fm}^3$  (which corresponds to an MSU strength of  $\text{Im}\{C_1\} = -0.54 \text{ fm}^6$ ) is added to the potential, in addition to the ELIV term. It is interesting to note that this additional term affects the forward cross sections of the light nuclei only moderately (and those of the heavy nuclei even less), and is relatively insignificant as compared to the effects of the ELIV term (see Fig. 3). The discrepancy between our calculation and the large-angle  $^{39}\text{K}$  data presumably results from the omission in our optical potential of nonzero multipole terms for  $J \neq 0$  nuclei, in this case a quadrupole term for a  $J = \frac{3}{2}$  nucleus.<sup>11</sup>

As for comparing our DCX calculations to data, the only low-energy angular distribution published at this time is for  $^{14}\text{C}$ . There are preliminary data from TRIUMF (Ref. 35) on  $^{18}\text{O}$  which are essentially the same as the  $^{14}\text{C}$  data. (Our DCX calculations of  $^{18}\text{O}$  are also essentially the same as the  $^{14}\text{C}$  results.) In Fig. 6 we compare our calculations to the  $^{14}\text{C}$  data. The solid and short-dashed curves are analog route calculations and correspond to the SCX curves in Fig. 5. For both of these calculations, the ELIV term is included in the isovector potential, but there is no isotensor potential. The isovector potential that yields the short-dashed curve differs from the one that yields the solid curve by the inclusion of the phenomenological isovector absorption-dispersive term  $\lambda_{p1}^{(2)}$  mentioned above. Although this term significantly altered the forward-angle  $^{14}\text{C}$  SCX results, it has a relatively mild effect on the corresponding DCX calculations. This indicates that variations in the magnitude of the analog route DCX cross sections are related to variations in the SCX cross sections over a relatively narrow angular region around 40–80 deg, which is understandable in lowest order ( $U_1 G U_1$ ) from the available phase space for the intermediate  $\pi^0$  angular integration. The long-dashed and dot-dashed curves are nonanalog route calculations which result from including the different isotensor potentials in addition to the isovector potential used to obtain the short-dashed curve. Inclusion of the ELIT term for the isotensor potential results in the long-dash curve. By comparing this curve to the analog route (short-dashed curve), we see that the ELIT term destructively interferes with the analog route amplitude. However, as noted in Sec. III, whether the correction is construc-

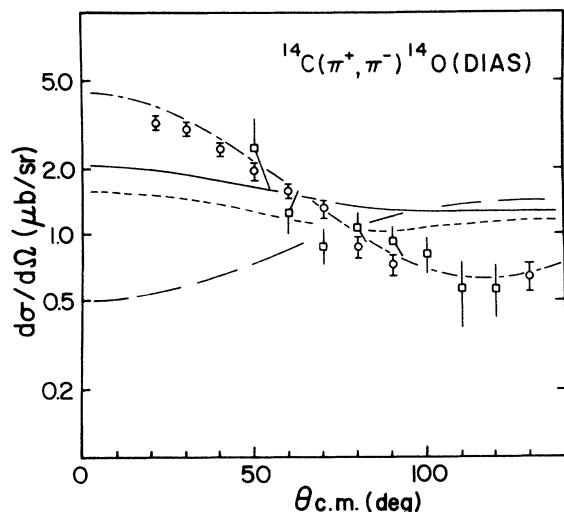


FIG. 6. Comparison of 50 MeV  $^{14}\text{C}(\pi^+, \pi^-)^{14}\text{O}(\text{DIAS})$  data (Ref. 2) to IICC calculations. Analog route calculations are shown with the ELIV term only (solid curve) and with, in addition, an imaginary second-order isovector  $p$ -wave term [ $\lambda_{p1}^{(2)} = (0 - 1.0i) \text{ fm}^{-3}$ ] (short-dashed curve). Also shown are calculations with both of the above higher-order isovector terms and the ELIT term (long-dashed curve) and with the ELIT term plus a real second-order isotensor  $p$ -wave term [ $\lambda_{p2}^{(2)} = (1.7 + 0i) \text{ fm}^{-3}$ ] (dot-dashed curve).

tive or destructive depends sensitively on short range correlations and intermediate distortions.

The DCX data shown in Fig. 6 indicates the need for a *constructive* interference between the isotensor potential and the analog route amplitude. Because all the  $p$ -wave correlation terms resulting from the EL effect are essentially real and negative [see Eqs. (3.3)], we can produce a constructive interference by including a positive real isotensor potential through the use of the  $p$ -wave isotensor absorption-dispersive term  $\Delta_{S_{p2}}^{(2)}$  given in Eq. (2.19). To accomplish this, we set the strength parameter in Eq. (2.19) to  $\text{Re}\lambda_{p2}^{(2)} = 1.7 \text{ fm}^3$ . The results of such an isotensor potential are shown by the dot-dashed curve, and indeed we see a constructive interference. From this calculational exercise, it appears that the ELIT term is an important correction for DCX, but the fact that the effect suppresses the cross section means that there are additional pieces affecting the DCX. Other effects that have been considered include sequential scattering via an intermediate nonanalog  $2^+$  state,<sup>13</sup> coupled-channel effects from including this nonanalog  $2^+$  state,<sup>36</sup> and six-quark cluster effects in the description of short-range N-N correlations.<sup>10</sup> It remains to be seen whether a theoretical description that includes all of the above effects is consistent with the data.

## V. DISTORTED WAVE APPROXIMATION TO CHARGE EXCHANGE

The striking results obtained in Sec. IV are analyzed further here, where we use a distorted wave Born approximation (DWBA) to the isospin-invariant coupled-channel (IICC) method of calculating charge exchange. Because

our calculational results indicated important sensitivities to the pion dynamics at low energy, we devote a substantial part of the discussion at the end of this section to show how this sensitivity arises. Within the DWBA, the physical origin of the effects is more easily visualized. Unlike the work of Ref. 6, in which a plane wave Born approximation (PWBA) was employed successfully to qualitatively describe low-energy elastic calculations, a PWBA does *not* resemble the IICC charge-exchange calculations on the data. The fact that the isoscalar potential is much larger than the isovector potential might lead one to suspect that higher-order terms in the Born series involving iterations of  $U_0$  must be included. Through the use of elastic distorted waves, the DWBA is a convenient way of understanding the effects of  $U_0$  on the IICC calculations of charge exchange.

The main points observed from the calculations discussed in this section are the following:

(1) The DWBA is an accurate approximation to the IICC calculations, and the DWBA enables Coulomb effects to be included. We find for SCX that Coulomb distortion effects are important at 50 MeV for  $Z \geq 20$ .

(2) By considering pion probability densities, we display the ability of pions to penetrate into the nucleus, and we see the increased penetration of 50-MeV pions relative to 165 MeV pions.

(3) Although 50-MeV distortions are weaker than those near the (3,3) resonance, they have a major influence in our model for SCX, and enhance the  $p$ -wave  $\pi$ -N transition amplitude relative to the  $s$ -wave part. The increased pion penetration of the nucleus at low energies allows medium modification to the reaction mechanism to contribute significantly. This leads to an energy- and  $A$ -dependent modification of the interference between the isovector  $s$ - and  $p$ -wave  $\pi$ -N amplitudes.

(4) Reasonable variations of the nuclear transition densities do not significantly alter the shape of the calculated SCX angular distributions, in contrast to the effect of changes in the second-order optical potential parameters. This implies that low-energy SCX may be a powerful tool for studying density-dependent medium modifications to the  $\pi$ -N interaction in nuclei.

The general matrix element for charge-exchange transitions from the nuclear ground state  $|g\rangle$  to the nuclear final state  $|f\rangle$  can be written for a zero-range  $\pi$ -N coupling as

$$\langle f: \pi^m, \mathbf{k}' | \hat{F} | g: \pi^+, \mathbf{k} \rangle = \int d\mathbf{r} \Psi_m^{(-)*}(\mathbf{k}', \mathbf{r}) \langle f | \hat{t}(\mathbf{r}) | g \rangle \Psi_+^{(+)}(\mathbf{k}, \mathbf{r}), \quad (5.1)$$

where  $\Psi_+^{(+)}$  ( $\Psi_m^{(-)}$ ) is the initial (final) distorted wave for the  $\pi^+$  ( $\pi^m$ ) of momentum  $\mathbf{k}$  ( $\mathbf{k}'$ ), and  $\langle f | \hat{t} | g \rangle$  is the nuclear matrix element of the appropriate charge-exchange transition operator. Because, for example, the difference between  $\pi^+$  elastic scattering from different isotopes is relatively small, the different isospin components of the optical potential are expected to satisfy the inequality  $U_0 \gg U_1 \gg U_2$ . In view of this we assume that the charge-exchange transition matrix may be obtained to a good approximation by using the lowest-order Born terms for the expression given in Eqs. (2.5). That is,

for SCX we assume

$$4\pi\langle f | \hat{t}(\mathbf{r}) | g \rangle^{\text{SCX}} = \sqrt{T_0}(F_1 - T_0 F_2) \simeq \sqrt{T_0} U_1, \quad (5.2)$$

and for DCX we assume

$$4\pi\langle f | \hat{t}(\mathbf{r}) | g \rangle^{\text{DCX}} = \sqrt{T_0(2T_0 - 1)} F_2 \\ \simeq \sqrt{T_0(2T_0 - 1)} (U_1 G U_1 + U_2). \quad (5.3)$$

For the purposes of this paper, we shall perform DWBA calculations for SCX only. By using the expressions given in Eqs. (2.10)–(3.3), we can factor out the isovector transition density and rewrite Eq. (5.2) in a form suitable for a distorted wave calculation:

$$\sqrt{T_0} U_1 = -(\bar{k}^2 V_1 + \nabla_{\pi'} \cdot V_2 \nabla_{\pi} + \frac{1}{2} \nabla^2 V_3) \left[ \frac{\Delta\rho}{2\sqrt{T_0}} \right] \quad (5.4a)$$

$$\simeq -\bar{k}^2 \left[ (V_1 - V_3) + (V_2 + V_3) \left[ \frac{\nabla_{\pi'} \cdot \nabla_{\pi}}{\bar{k}^2} \right] \right] \\ \times \left[ \frac{\Delta\rho}{2\sqrt{T_0}} \right], \quad (5.4b)$$

where  $\nabla_{\pi}$  ( $\nabla_{\pi'}$ ) operates on the initial (final) pion distorted wave,  $\bar{k}^2 = [(k')^2 + k^2]/2$ . The detailed expressions for the density dependent  $V$  coefficients are

$$V_1 = \bar{\lambda}_{s1}^{(1)} + \lambda_{s1}^{(2)} \left[ \frac{\rho}{\rho_0} \right], \quad (5.5a)$$

$$V_2 = \lambda_{p1}^{(1)} + \lambda_{p1}^{(2)} \left[ \frac{\rho}{\rho_0} \right] + L_1(\rho)\rho, \quad (5.5b)$$

$$V_3 = (p_1 - 1)\lambda_{p1}^{(1)} + (p_2 - 1)\lambda_{p1}^{(2)} \left[ \frac{\rho}{\rho_0} \right], \quad (5.5c)$$

with

$$\bar{\lambda}_{s1}^{(1)} \equiv \lambda_{s1}^{(1)} - \frac{3k^2}{8\pi^2 p_1} k_F [2\lambda_{s0}^{(1)} \lambda_{s1}^{(1)} - \frac{1}{2} (\lambda_{s1}^{(1)})^2],$$

and  $L_1(\rho)$  given in Eq. (3.3d). In our DWBA calculations we use Eq. (5.4a). The approximate Eq. (5.4b) is used in our pedagogical discussion at the end of the section.

In what follows we show DWBA calculations that result from using the above SCX transition matrix element. These calculations are performed with an extensively modified version of the computer code DWPI,<sup>37</sup> which numerically solves the Klein-Gordon equation to obtain the distorted waves for the complete elastic optical potential.

For our first study, we show in Fig. 7 a comparison between the DWBA and IICC calculations of SCX at 50 MeV. The only higher-order isovector term included in these calculations is the ELIV term. To make this comparison valid the Coulomb potential is not included in the calculation of the incident  $\pi^+$  distorted wave, and the energy of the final  $\pi^0$  is taken as the same as the  $\pi^+$  energy. The solid curves in this figure are the resulting DWBA calculations. The long-dashed curves are the same IICC results as in Fig. 3. By comparing the solid curves to the

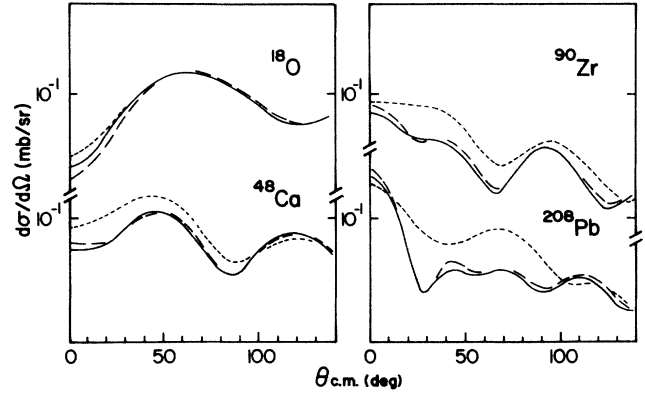


FIG. 7. Comparison of IICC and DWBA calculations at 50 MeV for several nuclei. The solid curve is a DWBA calculation with no Coulomb and with  $T_{\pi^+} = T_{\pi^0}$ . It is nearly identical to the IICC calculation (long-dashed curve). The short-dashed curve is the DWBA calculation with Coulomb included.

long-dashed curves, we see that for SCX the DWBA is an extremely accurate approximation to the IICC approach. This agreement also tells us something about the physics. The IICC approach differs from the DWBA in that the former proceeds through multiple transitions in and out of the IAS and DIAS. The latter, as we are using it, does not. The difference between the IICC and DWBA calculations is, presumably, a measure of the importance of such additional charge-exchange processes, and they are apparently negligible.

Because the DWBA does such a good job of describing the IICC calculations, we can use it to study the role of various effects which could not easily be isolated or included in the IICC framework. For example, one concern at low energies is the importance of Coulomb isospin-symmetry-breaking effects on SCX.<sup>19</sup> Within our DWBA, the importance of such effects can be easily assessed. The short-dashed curves in Fig. 7 are DWBA calculations which include Coulomb distortions on the incident  $\pi^+$  wave, but have no difference between the  $\pi^+$  and  $\pi^0$  kinetic energies. By comparing the solid curves to the short-dashed curves, we see that Coulomb distortion effects are negligible only for light nuclei, and these effects result in a general increase in the IICC calculated SCX cross sections. Calculations that include the appropriate IAS  $Q$ -value shifts give increases larger than those shown here. It is interesting to note from Fig. 5 that such effects will tend to improve the agreement between the <sup>48</sup>Ca calculations and the data.

A useful quantity that can be calculated from the distorted waves, and that will help to display the degree of pion penetration, is the pion probability density,

$$P_{\mathbf{k}}(\mathbf{r}) = |\Psi_{+}^{(+)}(\mathbf{k}, \mathbf{r})|^2. \quad (5.6)$$

This function is easy to visualize, and it qualitatively indicates the regions of the nucleus where reactions are most likely to occur. It also provides a useful means for comparing calculations that result from different theoretical models. In Fig. 8, we plot the 50-MeV  $\pi^+$  probability density surfaces for <sup>14</sup>C and <sup>48</sup>Ca. These surfaces result

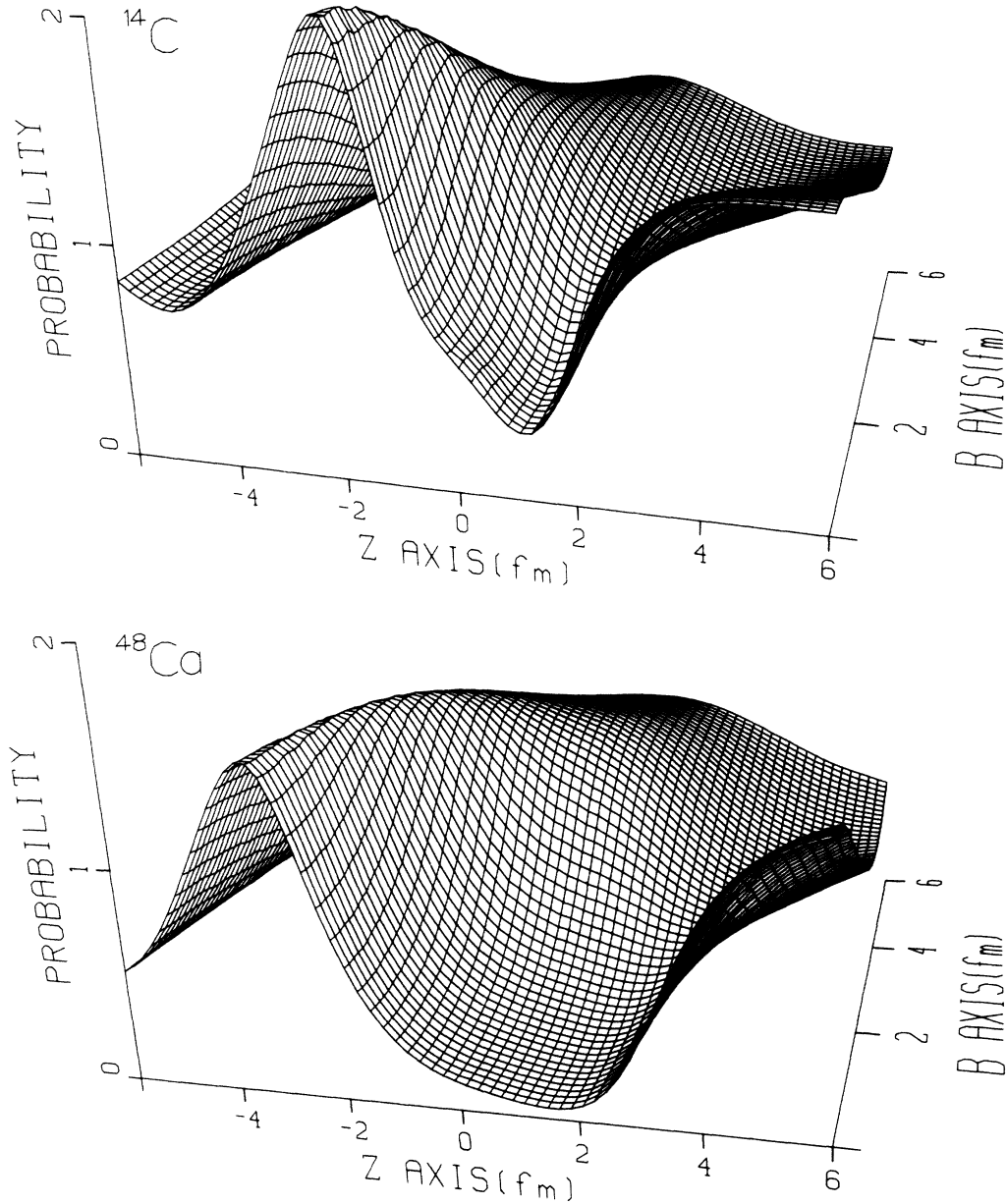


FIG. 8. 50-MeV  $\pi^+$  probability density surfaces for  $^{14}\text{C}$  and  $^{48}\text{Ca}$  resulting from the same optical potential used for the DWBA calculations shown in Fig. 7 (including Coulomb). The  $z$  axis is along the beam direction and the  $b$  axis represents impact parameter.

from the same optical potential that leads to the short-dashed curves (including Coulomb) in Fig. 7. The  $z$  axis is taken along the beam direction ( $\mathbf{k}$ ), with the origin at the center of the nucleus. The  $b$  axis is the impact parameter and corresponds to  $|\mathbf{r}|$  when  $\hat{\mathbf{k}} \cdot \hat{\mathbf{r}} = 0$ . The distorted waves are normalized to unity, and in the plane wave limit  $P(\mathbf{r}) = 1$ . From this figure we see that although the pion has some probability of penetrating into the center of light nuclei, the extent of this penetration decreases as the target size increases. We also see that there are interesting probability enhancements taking place in different regions of the nuclear surface. For example, in the  $z < 0$  region a bunching effect appears in front of the nucleus, and for

$z > 0$  a focusing effect appears behind the nucleus. Because these enhancements occur well within the nuclear half-way radius, one could speculate that specific inelastic transitions whose densities occupy the same regions of the nuclear surface may lead to inelastic cross sections that would be enhanced over their plane-wave values.

In Fig. 9 we show  $b=0$  probability slices for  $^{14}\text{C}$  and  $^{48}\text{Ca}$ . The curves in the top of Fig. 9 show the influence of various terms of the optical potential at 50 MeV. The solid curves at the top of Fig. 9 are identical to the  $b=0$  slices of the surfaces shown in Fig. 8, and result from the complete potential. The dotted curves at the top of Fig. 9 result from omitting the isoscalar and isovector

absorption-dispersive terms (i.e.,  $\lambda_{si}^{(2)} = \lambda_{pi}^{(2)} = 0$ ). In this case a significant probability enhancement appears near the center of the nucleus. From our complete calculations we find that the essential factor determining this enhancement, and thus the pion's ability to penetrate into the nucleus, is the isoscalar absorption-dispersive term. The dashed curves result from omitting the isoscalar and isovector EL terms ( $\alpha=0$ ) as well as the absorption-dispersive terms. These calculations are essentially first-order calculations. The singular points followed by the rapid decrease of probability in the nuclear interior results from the well-known Kisslinger catastrophe, where the effective in-medium wave number becomes imaginary. For some perspective, in the bottom of Fig. 9 we contrast the  $b=0$  probability slices for first-order optical potentials at 165 MeV (solid curves) and 100 MeV (dotted curves) to the 50-MeV dashed curves shown in the top of this figure. Of course near the (3,3) resonance, the first-order potential is dominated by the imaginary parts [e.g., at 165 MeV,  $\lambda_{p0}^{(1)} = (3.22 + 9.55i) \text{ fm}^3$  and  $\lambda_{p1}^{(1)} \simeq \lambda_{p0}^{(1)}$ ] and the strong attenuation of the pion flux is expected. However, at 100 MeV, where the real parts become appreciable [ $\lambda_{p0}^{(1)} = (8.67 + 3.96) \text{ fm}^3$  and  $\lambda_{p1}^{(1)} = (9.80 + 3.94i) \text{ fm}^3$ ], we can already see from the curves in the bottom of Fig. 9 the onset of the Kisslinger catastrophe. Furthermore, the first-order 165 MeV probability slices shown here are not appreciably different from those obtained with a potential that includes second-order terms adjusted to fit the data.<sup>17</sup> Thus, by comparing the solid curves in the top half of Fig. 9 to those in the bottom half, we can see how much further 50 MeV pions penetrate into the nuclear interior

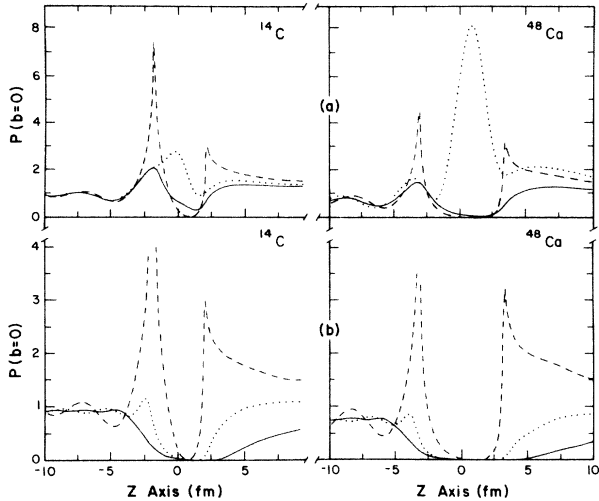


FIG. 9. Probability slices at  $b=0$  for  $\pi^+$  scattering on  $^{14}\text{C}$  and  $^{48}\text{Ca}$  from the same optical potential as in Fig. 8. The  $z$  axis is along the beam direction. In the top of this figure (a) 50-MeV slices are shown: the solid curves are  $b=0$  slices of the surfaces in Fig. 8 and result from the complete potential; the dotted curves result from omitting all absorption terms; and the dashed curves result from omitting the ELIS and ELIV terms as well (essentially first order). In the bottom (b), first-order slices are shown for 164 MeV (solid curves) and 100 MeV (dotted curves), along with those for 50 MeV (same as above—dashed curves).

than 165 MeV pions.

From the 50-MeV probability densities shown in Fig. 8, it is apparent that within our model, distorted waves are far from being plane waves. To understand in detail the quantitative effects of these distortions, we need to separate explicitly the distortion functions in the DWBA integrand. We accomplish this by performing the following manipulations. By inserting Eq. (5.4b) into (5.1), we write the distorted wave matrix element as

$$\langle \hat{F} \rangle^{\text{DW}} = - \frac{k^2}{8\pi\sqrt{T_0}} \int dr \Delta\rho(r) [W_s D_s(\mathbf{k}', \mathbf{k}; \mathbf{r}) + W_p D_p(\mathbf{k}', \mathbf{k}; \mathbf{r})], \quad (5.7)$$

where  $D_s$  and  $D_p$  are the  $s$ -wave and  $p$ -wave distortion functions,

$$D_s(\mathbf{k}', \mathbf{k}; \mathbf{r}) = \Psi^{(-)*}(\mathbf{k}', \mathbf{r}) \Psi^{(+)}(\mathbf{k}, \mathbf{r}), \quad (5.8a)$$

$$D_p(\mathbf{k}', \mathbf{k}; \mathbf{r}) = (k^{-2}) \nabla \Psi^{(-)*}(\mathbf{k}', \mathbf{r}) \cdot \nabla \Psi^{(+)}(\mathbf{k}, \mathbf{r}), \quad (5.8b)$$

and  $W_s = V_1 - V_3$ ,  $W_p = V_2 + V_3$  are the appropriate linear combinations of the density dependent  $V$  coefficients given in Eqs. (5.5). In these expressions we assume  $\bar{k}^2 \simeq k^2$  (i.e.,  $|\mathbf{k}'| \simeq |\mathbf{k}|$ ). Now because  $\Delta\rho$  in our calculations is a function of  $|\mathbf{r}|$ , Eq. (5.7) can be rewritten as

$$\langle \hat{F} \rangle^{\text{DW}} = - \frac{k^2}{2\sqrt{T_0}} \int dr [r^2 \Delta\rho(r)] [W_s d_s(\mathbf{k}', \mathbf{k}; r) + W_p d_p(\mathbf{k}', \mathbf{k}; r)], \quad (5.9)$$

where the radial distortion functions are defined as

$$d_i(\mathbf{k}', \mathbf{k}; r) = (4\pi)^{-1} \int d\Omega_r D_i(\mathbf{k}', \mathbf{k}; \mathbf{r}). \quad (5.10)$$

In the plane wave limit, i.e.,  $\Psi(\mathbf{k}, \mathbf{r}) \rightarrow \exp(i\mathbf{k} \cdot \mathbf{r})$ , the radial distortion functions are proportional to spherical Bessel functions of order  $l=0$ ,

$$d_s^{\text{PW}}(\mathbf{k}', \mathbf{k}; r) = j_0(qr) \quad (5.11)$$

and

$$d_p^{\text{PW}}(\mathbf{k}', \mathbf{k}; r) = \hat{\mathbf{k}}' \cdot \hat{\mathbf{k}} j_0(qr),$$

for the three-momentum transfer  $\mathbf{q} = \mathbf{k}' - \mathbf{k}$ . For the case of no distortions, Eq. (5.9) then gives the plane-wave amplitude

$$\langle \hat{F} \rangle^{\text{PW}} = - \frac{k^2}{2\sqrt{T_0}} \int dr [r^2 \Delta\rho(r)] [W_s + \hat{\mathbf{k}}' \cdot \hat{\mathbf{k}} W_p] j_0(qr). \quad (5.12)$$

If we make the additional restriction of omitting the density-dependent pieces from the  $W$  coefficients [ $\lambda^{(2)} = 0$ ,  $L_1 = 0$  in Eqs. (5.5)], Eq. (5.12) gives the plane-wave amplitude for a density-independent (PWDI) reaction mechanism,

$$\langle \hat{F} \rangle^{\text{PWDI}} = - \frac{k^2}{8\pi\sqrt{T_0}} \Delta\tilde{\rho}(q) \{ [\bar{\lambda}_{s1}^{(1)} - (p_1 - 1)\lambda_{p1}^{(1)}] + (p_1 \lambda_{p1}^{(1)}) \hat{\mathbf{k}}' \cdot \hat{\mathbf{k}} \}, \quad (5.13)$$

where  $\Delta\bar{\rho}(q)$  is the Fourier transform of  $\Delta\rho(r)$ . At  $q=0$ , this formula gives the very simple result for the  $\theta=0^\circ$  plane-wave density-independent cross section,

$$\frac{d\sigma^{\text{PWDI}}}{d\Omega}(k, \theta=0^\circ) = \frac{(N-Z)}{32\pi^2} k^4 |\bar{\lambda}_{s1}^{(1)} + \lambda_{p1}^{(1)}|^2, \quad (5.14)$$

which, because of normalization, is independent of  $\Delta\rho$ .

In Fig. 10 we show the real and imaginary parts of the  $\theta=0^\circ$  radial distortion functions [ $d_s$  and  $d_p$  of Eq. (5.10)] for 50-MeV  $\pi^+$  scattering from  $^{14}\text{C}$  and  $^{48}\text{Ca}$ . These curves are generated from the same optical potential used to obtain the solid curves in Fig. 7. We also show in the bottom of Fig. 10 the corresponding weighted transition densities,  $\delta(r) = r^2 \Delta\rho(r) / \sqrt{T_0}$ . The  $\delta(r)$ 's are important because they help to select the regions of the nuclear radii that contribute to the radial integrals. Note that in the regions selected by the  $\delta(r)$ 's,  $d_s$  and  $d_p$  differ from each other and from the plane-wave values ( $d = 1.0 + 0.0i$ ). These differences, particularly in the imaginary parts, play an important role in understanding the effects of distortions and their influence upon the cancellation between components of the transition operator. We use Eqs. (5.9)–(5.14), along with the curves in Fig. 10, to discuss the following results.

We now demonstrate the influence of the distorted waves by contrasting, in Figs. 11(a) and (b), The DWBA results (solid curves) to the PWBA results (dashed curves) for  $^{14}\text{C}$  and  $^{48}\text{Ca}$ . The potential that determines the distorted waves in this figure is the complete potential used to calculate the solid curve DWBA results shown in Fig.

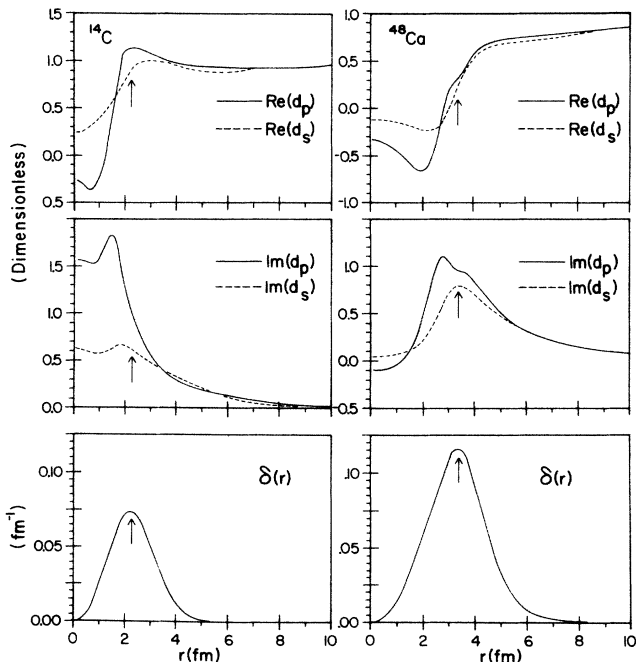


FIG. 10. Real (top curves) and imaginary (center curves) parts of the  $\theta=0$  radial distortion functions for 50 MeV  $\pi^+$  elastic scattering from  $^{14}\text{C}$  (left side) and  $^{48}\text{Ca}$  (right side of the figure). Curves at the bottom are the corresponding weighted transition densities.

7. The inelastic transition operator for the calculations in Fig. 11(a) does not include any isovector absorption-dispersive terms or the ELIV term [i.e., in Eqs. (5.5)  $\lambda^{(2)}=0$ ,  $L_1=0$ ] and is, therefore, density independent. However in Fig. 11(b), the inelastic transition operator does include the  $p$ -wave isovector absorption-dispersive term ( $\lambda_{p1}^{(2)} = -1.0i \text{ fm}^3$ ) and the ELIV term ( $\alpha=1.6$ , so that  $L_1 \neq 0$ ). From the curves shown in Fig. 11, we observe the following features.

In Fig. 11(a), the forward-direction PWBA results strongly resemble the nonspin flip part of the free  $\pi$ -N cross section (depicted in Fig. 12 as the solid curve). This indicates that the effects of the  $s$ -wave correlation term [the  $k_F$  term in Eq. (5.5a)] and the Pauli blocking of the imaginary parts of the  $\lambda^{(1)}$ 's do not appreciably alter the cancellation taking place between the  $s$ - and  $p$ -wave isovector nonspin flip term around  $30^\circ$ . In this angular region, the free  $\pi$ -N process is dominated by the spin flip contribution as shown by the dashed curve in Fig. 12, which includes both the spin flip and nonspin flip amplitudes. Of course, for  $J=0$  nuclei, the IAS transition precludes any spin flip contribution in lowest order. The exact position in angle (and in energy) of the  $s$ - $p$  interference for the  $\pi$ -N charge-exchange process depends on the model used to obtain the  $\pi$ -N phase shifts. In this low-energy region, the phase shifts are not extremely well known at this time. The model we are using [Ref. 24] does a reasonably good job of describing the new

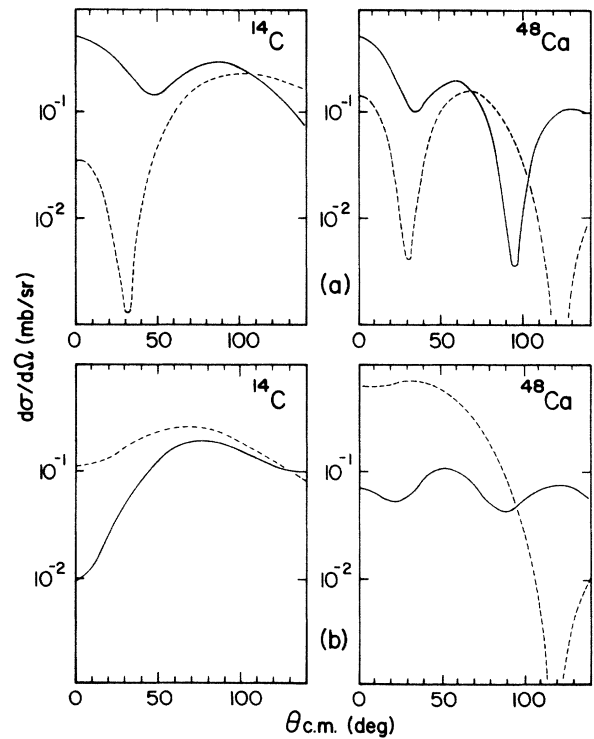


FIG. 11. DWBA (solid curves) and PWBA (dashed curves) calculations for 50 MeV SCX to the IAS on  $^{14}\text{C}$  and  $^{48}\text{Ca}$ . In (a) no ELIV and no isovector absorption terms are included (density-independent reaction mechanism) while in (b) both an isovector  $p$ -wave absorption term [ $\lambda_{p1}^{(2)} = (0 - 1.0i) \text{ fm}^3$ ] and the ELIV term are included (density-dependent reaction mechanism).

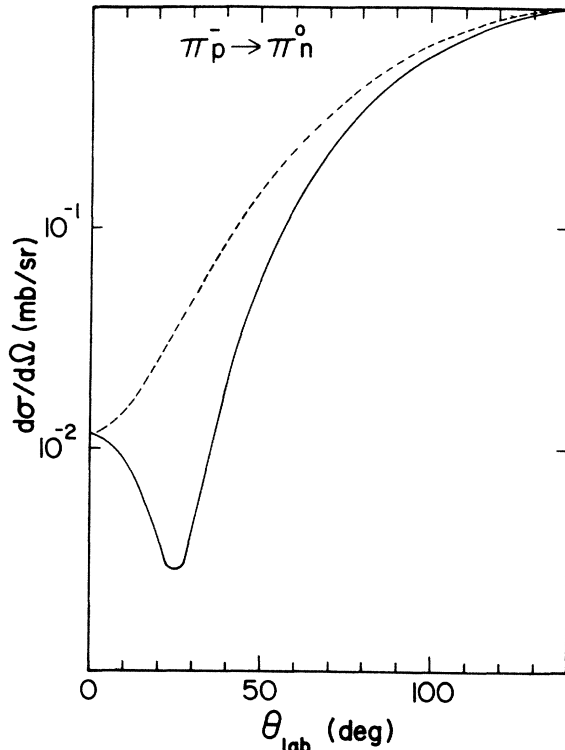


FIG. 12. The free  $\pi^-p \rightarrow \pi^0n$  angular distribution at 50 MeV from the phase-shift solution "C5" of Arndt (Ref. 24). The solid curve is without the spin-flip part and the dashed curve is with it.

forward-angle data at 50 MeV,<sup>38</sup> but it does not accurately describe the energy dependence.

We also note, by comparing the PWBA results (dashed-curves) of Fig. 11(b) to those of Fig. 11(a), that the decrease of the isovector  $p$ -wave attraction resulting from the inclusion of the ELIV term greatly reduces the destructive  $s$ - $p$  interference. Additional PWBA calculations resulting from the omission of  $\text{Im}\lambda_{p1}^{(2)}$  cannot be distinguished from the plotted dashed curves which include  $\text{Im}\lambda_{p1}^{(2)}$ . As we show below, this cancellation takes place in the real parts of the amplitudes.

Finally we note that the role of distortion effects changes between Figs. 11(a) and (b). In Fig. 11(a) distortions significantly increase the forward cross sections, whereas in Fig. 11(b) they significantly decrease the forward cross sections.

The calculations shown in Fig. 11(a) result from a density-independent reaction mechanism. To understand the plane-wave results (dashed curves) in this figure we use the PWDI formulas given by Eqs. (5.13) and (5.14). We first note that the zero-degree cross sections for  $^{48}\text{Ca}$  and  $^{14}\text{C}$  differ by a factor of 4, reflecting the  $N$ - $Z$  dependence of Eq. (5.14). To a good approximation, the average  $\lambda^{(1)}$ 's for  $^{48}\text{Ca}$  and  $^{14}\text{C}$  may be taken as purely real,  $\bar{\lambda}_{s1}^{(1)} \simeq -9.08 \text{ fm}^3$  and  $\lambda_{p1}^{(1)} \simeq 10.84 \text{ fm}^3$ . By using these values in Eq. (5.14), the absolute magnitudes of the zero-degree cross sections are well reproduced. The first minimum in the plane-wave curves of Fig. 11(a) can be

obtained by finding the zero of the reaction mechanism part of Eq. (5.13), i.e.,

$$\cos\theta_{\min} = [(p_1 - 1)\lambda_{p1}^{(1)} - \bar{\lambda}_{p1}^{(1)}].$$

For the average value of  $p_1 = 1.19$  and for the approximate values of the  $\lambda^{(1)}$ 's given above,  $\theta_{\min} \simeq 30^\circ$ . The additional minima in these plane wave curves result from the nuclear form factors  $\Delta\bar{\rho}(q)$ .

The striking feature of the distorted-wave results (solid curves) in Fig. 11(a) is the large increase over the plane-wave results in the forward direction. To understand this behavior, we use Eq. (5.9) to approximate the ratio of zero-degree distorted wave to plane-wave cross sections as

$$R = \frac{|W_s \bar{d}_s + W_p \bar{d}_p|^2}{|W_s + W_p|^2}, \quad (5.15)$$

where in this expression the  $\bar{d}$ 's are the average values of the radial distortion functions. In general (and particularly at higher energies), the point that determines these average distortion functions does not coincide with the point at which the  $\delta(r)$ 's peak. However, for the purpose of this discussion, and because of the increased penetration at low energies, we find it useful to determine the average distortion functions over the region of nuclear radius for which the  $\delta(r)$ 's peak. From Fig. 10, we see that for  $^{14}\text{C}$  this region is around  $r \simeq 2.2 \text{ fm}$  and for  $^{48}\text{Ca}$  it is around  $3.4 \text{ fm}$ . These radii correspond to approximately the 80% density point in  $^{14}\text{C}$  and the 60% density point in  $^{48}\text{Ca}$ . The vertical arrows in this figure indicate these positions, where we find for  $^{14}\text{C}$ ,  $\bar{d}_s \simeq 0.9 + 0.6i$  and  $\bar{d}_p \simeq 1.1 + 1.0i$ ; and for  $^{48}\text{Ca}$ ,  $\bar{d}_s \simeq 0.2 + 0.8i$  and  $\bar{d}_p \simeq 0.3 + 1.0i$ . With the values of the  $\lambda^{(1)}$ 's given above, the density independent  $W$ 's have the values  $W_s \simeq -11.1 \text{ fm}^3$  and  $W_p \simeq +12.9 \text{ fm}^3$ . Inserting these values into Eq. (5.15) we obtain  $R(^{14}\text{C}) \simeq 18$  and  $R(^{48}\text{Ca}) \simeq 6$ , which are qualitatively the same as the observed calculational results. Thus, we see how the differences between the  $s$ -wave and  $p$ -wave distortion functions alter the  $s$ - $p$  interference of the plane-wave reaction mechanism and yield large forward-angle cross sections. Note that such large ratios result even though  $\bar{d}_s$  and  $\bar{d}_p$  are close to being the same. This is a demonstration of the sensitivity of cross sections to details of the theory. One may therefore regard the existence of the interference as a tool to be exploited for the purpose of probing the density dependence of the  $\pi$ - $A$  interaction mechanism.

The calculations shown in Fig. 11(b) result from a density-dependent reaction mechanism that includes the  $p$ -wave isovector absorption-dispersive term ( $\lambda_{p1}^{(2)} = -1.0i \text{ fm}^3$ ) and the ELIV term ( $L_1 \neq 0$ ) in Eq. (5.5b). The effect of these terms is to decrease  $W_p$  from its density-independent value: the ELIV term is essentially real and therefore decreases the  $p$ -wave attraction, whereas the  $\lambda_{p1}^{(2)}$  term adds a small negative imaginary term. If we let  $\bar{W}_p$  be the average value of the density dependent  $W_p$ , we find at the 80% and 60% density points [corresponding to the radii at which the  $\delta(r)$ 's peak] the effective values of  $\bar{W}_p \simeq (7.1 - 0.72i) \text{ fm}^3$  and  $\bar{W}_p \simeq (8.6 - 0.45i) \text{ fm}^3$ , respectively. By comparing these values to the  $W_s \simeq -11.1 \text{ fm}^3$ , we see from Eq. (5.13) that the real part of  $W_s + \cos\theta \bar{W}_p$

can never vanish, and therefore the inclusion of the ELIV eliminates the dramatic forward-angle  $s$ - $p$  cancellation.

To understand the distortion effects in Fig. 11(b), where the DWBA calculations (solid curves) for the density-dependent reaction mechanism are significantly smaller than the PWBA results (dashed curves), we again use the approximate ratio given by Eq. (5.15). For the values of  $\bar{d}_s$ ,  $\bar{d}_p$ ,  $W_s$ , and  $W_p$  given above, we find  $R(^{14}\text{C}) \simeq 0.14$  and  $R(^{48}\text{Ca}) \simeq 0.13$ , which qualitatively describe the forward-angle reductions seen in the calculations. In this case, where there is no  $s$ - $p$  cancellation between  $W_s$  and  $W_p$  in the reaction mechanism, the differences between the distortion functions  $\bar{d}_s$  and  $\bar{d}_p$  tend to cause a cancellation, i.e.,  $|W_s \bar{d}_s + W_p \bar{d}_p| < |W_s + W_p|$ . These results are interesting because they demonstrate that the significant influence of distortion effects on low-energy SCX calculations results from the *difference* between the  $s$ -wave and  $p$ -wave distortion functions.

Because the relative weighting of the  $s$ - and  $p$ -wave distortion functions is essentially determined by the transition density through the function  $\delta(r)$ , we expect our calculations to be sensitive to variations in the transition densities. We quantitatively demonstrate the degree of sensitivity in Fig. 13, where we show 50-MeV DWBA calculations of SCX for  $^{14}\text{C}$  and  $^{48}\text{Ca}$  that result from using two different models for the transition densities [ $\Delta\rho$  in Eq. (5.4)]. The solid curves in Fig. 13(a) are the same as those of Fig. 11 and result from the  $N/Z$  scaling model for  $\Delta\rho$ .

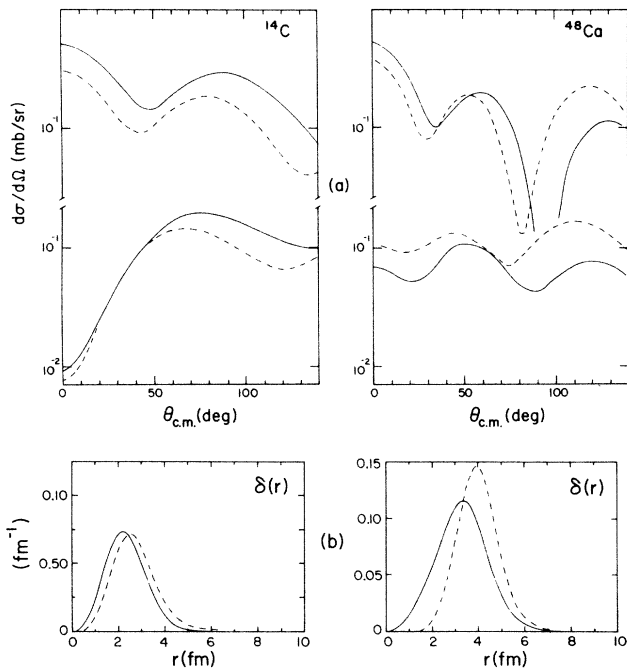


FIG. 13. 50-MeV DWBA calculations of SCX for  $^{14}\text{C}$  and  $^{48}\text{Ca}$ , where the solid curves use  $N/Z$  densities and the dashed curves are with Hartree-Fock densities. The top pair of curves in (a) result from the density-independent reaction mechanism and the lower curves result from the density-dependent one (as in Fig. 11). In (b) the corresponding  $N/Z$  (solid) and Hartree-Fock (dashed) weighted transition densities are shown.

The dashed curves result from using excess neutron densities obtained from Hartree-Fock (HF) calculations with a Skyrme III force.<sup>39</sup> The corresponding  $\delta(r)$ 's are shown in Fig. 13(b): the solid curves are the  $N/Z$  model (also shown in Fig. 10), and the dashed curves are the HF results.

As in Fig. 11, the cross sections in the top (bottom) half of Fig. 13(a) are calculated by using a density-independent (-dependent) reaction mechanism that results from omitting (including) the isovector absorption-dispersive and ELIV terms. We see that for the density-independent reaction mechanism, the use of the HF model lowers the forward angle cross sections. In contrast, the density-dependent reaction mechanism calculations show very little forward-angle sensitivity for  $^{14}\text{C}$ , while for  $^{48}\text{Ca}$  the use of the HF model increases the cross section. We note that the overall effect of using HF densities does not significantly alter the qualitative shape of the calculations, and we conclude that density-dependent reaction mechanism effects are required to reproduce the forward-angle interference.

We can explain the above SCX cross-section dependences on the nuclear wave functions by considering the shift in position for which the HF  $\delta(r)$ 's reach their maxima. From Fig. 13(b), we see that for  $^{14}\text{C}$  the HF model moves the position of the  $\delta(r)$ 's peak from  $r(N/Z) \simeq 2.2$  fm to  $r(\text{HF}) \simeq 2.5$  fm, whereas for  $^{48}\text{Ca}$  the peak position moves from  $r(N/Z) \simeq 3.4$  fm to  $r(\text{HF}) \simeq 4.0$  fm. These HF values of radii corresponds to approximately the 60% density point in  $^{14}\text{C}$  and the 40% density point in  $^{48}\text{Ca}$ . Now by using Fig. 10 to obtain the new average distortion functions evaluated at these new peak positions, we find for  $^{14}\text{C}$ ,  $\bar{d}_s^{\text{HF}} \simeq 1.0 + 0.6i$  and  $\bar{d}_p^{\text{HF}} \simeq 1.1 + 0.8i$ ; and for  $^{48}\text{Ca}$ ,  $\bar{d}_s^{\text{HF}} \simeq 0.50 + 0.70i$  and  $\bar{d}_p^{\text{HF}} \simeq 0.55 + 0.85i$ . From the values of the  $N/Z$  average distortion functions ( $\bar{d}$ 's) and the reaction mechanism  $W$ 's given above we can form a ratio analogous to Eq. (5.15), i.e.,

$$R' = \frac{|W_s \bar{d}_s^{\text{HF}} + W_p \bar{d}_p^{\text{HF}}|^2}{|W_s \bar{d}_s + W_p \bar{d}_p|^2}, \quad (5.16)$$

in order to estimate the effects of the HF densities on the zero-degree cross sections.

For the density-independent values of  $W_s \simeq -11.1 \text{ fm}^3$  and  $W_p \simeq 12.9 \text{ fm}^3$ , Eq. (5.16) gives us  $R'(^{14}\text{C}) \simeq 0.4$  and  $R'(^{48}\text{Ca}) \simeq 0.7$ , which qualitatively describes the calculated ratios in the top half of Fig. 13(a). We can also estimate the ratio of cross sections for the density-dependent reaction mechanism by replacing the  $W_p$ 's evaluated at the appropriate density points. In addition to the  $W_p$  values quoted above for the 80% and 60% density points, we now also need the effective value at the 40% density point,  $W_p \simeq 10.5 \text{ fm}^3$ . We note that the HF values of  $W_p$  are to be taken at values different from those for the  $N/Z$  case: For  $^{14}\text{C}$ , the density-dependent ratio is calculated with the numerator evaluated at the 60% HF value of  $W_p$  and the denominator at the 80% ( $N/Z$ ) value. For  $^{48}\text{Ca}$ , the numerator is evaluated at the 40% (HF) value of  $W_p$  and the denominator at the 60% ( $N/Z$ ) value. By using the appropriate values of  $W_p$ , the density-dependent ratios become  $R'(^{14}\text{C}) \simeq 0.8$  and  $R'(^{48}\text{Ca}) \simeq 1.7$ , which describes

the calculated forward-angle ratios shown in the bottom half of Fig. 13(b). This analysis underscores the fact that distortion effects play a very important role in our model of SCX, with the mean density of interaction being roughly 50% of the central density.

## VI. SUMMARY AND CONCLUSIONS

The purpose of this paper is to determine the implications of nuclear correlations on low-energy pion charge exchange; such correlations were previously found to be necessary to describe elastic scattering at these energies. To attain this goal, we assume an isospin-invariant optical-potential framework that explicitly couples the nuclear ground state to the isobaric analog states, and that provides a unified approach to pion-nucleus isoelastic scattering. We refer to this framework as the isospin-invariant coupled-channel (IICC) framework. Within this framework, theories of elastic scattering can be used to calculate charge exchange, provided that the isospin components of the potential are given.

The particular form of the potential we adopted was motivated by two main considerations: it was shown to be successful at higher energies, and it is similar in form to a successful potential for low-energy elastic scattering (the MSU potential). In constructing the isospin components of this potential, we explicitly separated the first-order terms (those linear in the density) from the higher-order terms. Effects contributing to these higher-order terms were divided into two pieces: one associated with  $\pi$ -2N absorption and dispersive effects, and the other with correlations. The quantities governing the strength of the first-order terms were determined from the  $\pi$ -N phase shifts. The form of the correlation terms and the quantities governing their strength were also theoretically determined. The absorption-dispersive terms were considered as phenomenological, with the isoscalar strengths fixed from the analysis of elastic scattering and pionic atoms, and the isovector and isotensor strengths to be determined from SCX and DCX data. In the calculations reported here, we show that only two real parameters (of reasonable strength) are needed to give a good description of the SCX and DCX data at 50 MeV. The details of the potential are summarized at the beginning of Sec. IV, and the parameters for 50 MeV are given in Table II.

One of the most significant effects observed in the IICC calculations (shown in Sec. IV) is the influence of the  $p$ -wave isovector correlation (ELIV) term on SCX. Without this term, the calculated cross sections are strongly forward peaked, in contrast to the deep forward dip of the elementary  $\pi$ -N cross section. The inclusion of this correlation term dramatically reduced the differential cross sections, particularly for light nuclei, where forward maxima became forward minima. Comparison of these calculations to the available SCX data near 50 MeV clearly supports the need for such an isovector correlation term in the optical potential.

Because the potential used in our calculations was based upon the well-established MSU elastic scattering model, our findings lend further weight to the conclusion that short-range correlations, rho-meson exchange, and Pauli

correlations consistently play a necessary role in the description of low-energy pion-nucleus scattering. One should therefore be skeptical of calculations that achieve agreement with the data without including these correlation effects.

The inclusion of  $p$ -wave correlations also significantly affected the IICC calculations of DCX cross sections. For analog route calculations (i.e., no isotensor potential), we found large differences between predicted DCX cross sections that included isovector correlations and those that omitted this term. The influence of the corresponding isotensor correlation (ELIT) term on DCX was smaller, and interfered destructively with the analog route amplitude. Comparison of these calculations to the limited available DCX data supports the existence of the isovector correlated analog route to DCX, but indicates that another process is required to yield a constructive interference between the isotensor term and this analog route amplitude.

To gain insight into the IICC calculations, we also formulated a distorted-wave Born approximation that accurately reproduced the IICC results for SCX. The DWBA allowed us to study separately the effects of elastic distortion and nuclear-medium modifications to the isovector transition operator. The DWBA also enabled us to study Coulomb distortions and other isospin-symmetry-breaking effects that may be significant for low-energy charge exchange on medium to heavy nuclei. Because of these findings, we conclude that our DWBA approach (at least for low-energy SCX) is more flexible, and therefore may be more desirable for future calculations than the IICC approach. We stress that the transition operator used has been renormalized by medium effects, which is essential. Encouraged by these results, we are currently investigating the replacement of IICC calculations of DCX by a similar DWBA for DCX.

Our DWBA studies (presented in Sec. V) reveal that elastic distortion effects on low-energy SCX calculations are substantial for the MSU potential model. This stems from the fact that the scalar and gradient distortion functions associated with the  $s$ - and  $p$ -wave parts of the transition operator differ from each other, and thereby alter the free-space  $s$ - $p$  interference in the isovector channel. When the free-space  $\pi$ -N transition operator (i.e., the impulse approximation) is used, the alteration of the  $s$ - $p$  interference caused by the distortions give forward-peaked angular distributions. Including the density-dependent modifications to the isovector transition operator that resulted from  $p$ -wave correlations causes the DWBA calculations to decrease, and to come in line with the data. The significant differences between DWBA and plane wave calculations (shown in Sec. V) also indicate that plane-wave arguments may not be very reliable for the discussion of low-energy charge exchange. We find from these studies that the mean density of interaction is roughly 50% of the central density.

There are many interesting future directions that may be used to test the relatively simple model proposed in this paper. We have shown that this model can successfully describe the  $A$  dependence of isoelastic scattering near 50 MeV. The next step is to study its ability to describe the

energy dependence of the isoelastic cross sections throughout the low-energy regime. For example, after adjusting the absorption-dispersive parameters to fit a few targets, or calculating them from theory, it would be interesting to see if the model can successfully predict the  $\pi^+$  and  $\pi^-$  elastic scattering from various isotopes as well as SCX and DCX. From such energy-dependent studies, one would be able to investigate the role of the  $s$ - $p$  interference in SCX and its movement away from forward angles. Additional tests can be made by studying the isospin dependence of pion absorption data and pionic atoms. Inelastic scattering to various selected states also offers us the opportunity to selectively test various components of the correlation-induced density-dependent transition operator. We look forward to testing this model against future planned experiments, and, perhaps, to establish a relatively simple characterization of the low-energy pion-nucleus interaction.

#### ACKNOWLEDGMENTS

We thank the local staff members and visitors of the Medium Energy Physics and Theoretical divisions of the Los Alamos National Laboratory for many useful discussions relating to this subject, especially N. Auerbach, H. W. Baer, G. E. Brown, W. R. Gibbs, and P. B. Siegel. One of us (E.R.S.) is grateful to L. Rosen for his kind hospitality at LAMPF and to the Atomic and Molecular Physics Group at the University of Georgia for the use of their computing resources. This work was supported in part by the U.S. Department of Energy.

#### APPENDIX A: ISOSPIN-INVARIANT COUPLED EQUATIONS

To obtain the coupled equations for the isoscalar, isovector, and isotensor components ( $F_i$ ,  $i=0,1,2$ ) of the transition operator in terms of the optical potential isospin components ( $U_i$ ), we first introduce the isospin operator identity

$$(\phi \cdot \mathbf{T})^3 = -2(\phi \cdot \mathbf{T})^2 + (\phi \cdot \mathbf{T})[(\mathbf{T})^2 - 1] + \frac{1}{2}(\phi)^2(\mathbf{T})^2, \quad (\text{A1})$$

where  $\phi$  ( $\mathbf{T}$ ) is the pion (nuclear) isospin operator. This identity follows from the fact that the components of  $\phi$  are  $3 \times 3$  Hermitian matrices that form the three-dimensional representation of the SU(2) rotation group, i.e.,

$$W = \begin{pmatrix} U_0 & T_0(T_0+1)U_2 & T_0(T_0+1)(U_1-2U_2) \\ U_1 & U_0+(T_0^2+T_0-1)U_2 & (T_0^2+T_0-1)U_1+(2-T_0^2-T_0)U_2 \\ U_2 & U_1-2U_2 & U_0-2U_1+(T_0^2+T_0+3)U_2 \end{pmatrix}.$$

A transformation from the above basis of scalar, vector, and tensor components (indicated by the indices  $i=0,1,2$ ) to the basis of total isospin (indicated by the indices  $I=T_0+1, T_0, T_0-1$ ) can be made through the use of

$$\phi_x = \frac{1}{\sqrt{2}} \begin{pmatrix} 0 & 1 & 0 \\ 1 & 0 & 1 \\ 0 & 1 & 0 \end{pmatrix},$$

$$\phi_y = \frac{i}{\sqrt{2}} \begin{pmatrix} 0 & -1 & 0 \\ 1 & 0 & -1 \\ 0 & 1 & 0 \end{pmatrix},$$

$$\phi_z = \begin{pmatrix} 1 & 0 & 0 \\ 0 & 0 & 0 \\ 0 & 0 & -1 \end{pmatrix}.$$

From this representation one can show that these operators satisfy the usual angular momentum commutation rule

$$\phi_j \phi_k - \phi_k \phi_j = i \epsilon_{jkl} \phi_l,$$

as well as the rule

$$\phi_j \phi_k \phi_l + \phi_l \phi_k \phi_j = \delta_{jk} \phi_l + \delta_{lk} \phi_j.$$

For more discussion about this representation, see, for example, Ref. 40.

The identity given in Eq. (A1) is important because it enables us to show that powers of the pion isospin operator greater than two are reducible. For example, by multiplying Eq. (A1) by  $\phi \cdot \mathbf{T}$  we obtain

$$(\phi \cdot \mathbf{T})^4 = (\phi \cdot \mathbf{T})^2[(\mathbf{T})^2 + 3] + (\phi \cdot \mathbf{T})\{(\mathbf{T})^2[\frac{1}{2}(\phi)^2 - 2] + 2\} - (\phi)^2(\mathbf{T})^2. \quad (\text{A2})$$

This multiplicative procedure can be continued, yielding the general result

$$(\phi \cdot \mathbf{T})^n = (\phi \cdot \mathbf{T})^2 a_n + (\phi + \mathbf{T}) b_n + c_n, \quad (\text{A3})$$

where  $a_0 = b_0 = 0$ ,  $c_0 = 1$ ;  $a_1 = c_1 = 0$ ,  $b_1 = 1$ ;  $a_2 = 1$ ,  $b_2 = c_2 = 0$ ; and by using the eigenvalues of  $(\phi)^2$  and  $(\mathbf{T})^2$ ,  $a_3 = -2$ ,  $b_3 = T_0(T_0+1)-1$ ,  $c_3 = T_0(T_0+1)$ . The coefficients for  $n > 3$  can be obtained through the recurrence relations  $a_n = a_{n-1}a_3 + b_{n-1}$ ,  $b_n = a_{n-1}b_3 + c_{n-1}$ ,  $c_n = a_{n-1}c_3$ .

Now by using Eqs. (A1) and (A2), we can obtain the desired equations for the  $F_i$ 's in terms of the  $U_i$ 's. By inserting the isospin decompositions for  $\hat{U}$  and  $\hat{F}$  given by Eqs. (2.1) and (2.4) into Eq. (2.3), and by using the identities in Eqs. (A1) and (A2) with  $(\phi)^2$  and  $(\mathbf{T})^2$  replaced by their eigenvalues, we find

$$F_i = U_i + \sum_{j=0,1,2} W_{ij} G F_j, \quad (\text{A4})$$

where the coupling matrix is given by

the projection operators

$$\Omega_{T_0+1} = \frac{(1 + \phi \cdot \mathbf{T})(1 + T_0 + \phi \cdot \mathbf{T})}{(T_0 + 1)(2T_0 + 1)},$$

$$\Omega_{T_0} = \frac{(T_0 - \boldsymbol{\phi} \cdot \mathbf{T})(1 + T_0 + \boldsymbol{\phi} \cdot \mathbf{T})}{T_0(T_0 + 1)}, \quad (\text{A5})$$

$$\Omega_{T_0-1} = \frac{(1 + \boldsymbol{\phi} \cdot \mathbf{T})(\boldsymbol{\phi} \cdot \mathbf{T} - T_0)}{T_0(2T_0 + 1)},$$

which can be shown to satisfy the usual idempotent property  $\Omega_I \Omega_{I'} = \delta_{II'} \Omega_I$ . With these projection operators,  $\hat{U}$  and  $\hat{F}$  can be resolved onto total isospin components  $U_I$  and  $F_I$ , as indicated by the expressions in Eq. (2.8). By inserting these expressions for  $\hat{U}$  and  $\hat{F}$  into Eq. (2.3), and by using the fact that  $G$  commutes with the  $\Omega_I$ 's, we find the relation between the  $F_I$ 's and the  $U_I$ 's to be diagonal in the channel indices, i.e.,  $F_I = U_I(1 + GF_I)$ . The specific transformation matrix that relates the two bases is

$$M = \begin{pmatrix} 1 & T_0 & T_0^2 \\ 1 & -1 & 1 \\ 1 & -(T_0 + 1) & (T_0 + 1)^2 \end{pmatrix}, \quad (\text{A6})$$

where, for example,

$$U_I = \sum_{i=0,1,2} M_{Ii} U_i.$$

The inverse transformation is obtained, of course, by inverting  $M$ .

#### APPENDIX B: RELATIONS OF PARAMETERS TO PHASE SHIFTS AND THE MSU NOTATION

The first-order coupling coefficients (the  $\lambda^{(1)}$ 's) are obtained from the  $\pi$ -N phase shifts  $\delta(\kappa)$  by means of the following relations:

$$\lambda_{s0}^{(1)} = \frac{4\pi(2\gamma_3 + \gamma_1)p_1}{(3\kappa k^2)},$$

$$\lambda_{s1}^{(1)} = \frac{8\pi(\gamma_3 - \gamma_1)p_1}{(3\kappa k^2)},$$

$$\lambda_{p0}^{(1)} = \frac{4\pi(4\gamma_{33} + 2\gamma_{31} + 2\gamma_{13} + \gamma_{11})}{(3p_1\kappa^3)},$$

$$\lambda_{p1}^{(1)} = \frac{8\pi(2\gamma_{33} - 2\gamma_{31} + \gamma_{13} - \gamma_{11})}{(3p_1\kappa^3)}, \quad (\text{B1})$$

where for  $s$  waves ( $\gamma_{2T}$ ) and for  $p$  waves ( $\gamma_{2I,2T}$ ),  $\gamma(\kappa) = \exp[i\delta(\kappa)]\sin\delta(\kappa)$ , and  $\kappa$  is the wave number in the  $\pi$ -N center-of-momentum frame. Note that the frame transformation parameter  $p_1$  is included in the definitions of the  $\lambda^{(1)}$ 's. These first-order quantities are related to the MSU first-order terms  $b_0$ ,  $b_1$ ,  $c_0$ , and  $c_1$  as follows:

$$b_0 = \lambda_{s0}^{(1)} \left[ \frac{k^2}{4\pi p_1} \right],$$

$$b_1 = \lambda_{s1}^{(1)} \left[ \frac{k^2}{8\pi p_1} \right],$$

$$c_0 = \lambda_{p0}^{(1)} \left[ \frac{p_1}{4\pi} \right], \quad (\text{B2})$$

$$c_1 = \lambda_{p1}^{(1)} \left[ \frac{p_1}{8\pi} \right].$$

In these expressions  $k$  is the pion wave number in the  $\pi$ - $A$  center-of-momentum frame. The following expressions relate the second-order MSU parameters  $B_0$ ,  $B_1$ ,  $C_0$ , and  $C_1$  to the  $\lambda^{(2)}$ 's:

$$B_0 = \lambda_{s0}^{(2)} \left[ \frac{k^2}{4\pi p_2 \rho_0} \right],$$

$$B_1 = \lambda_{s1}^{(2)} \left[ \frac{k^2}{8\pi p_2 \rho_0} \right], \quad (\text{B3})$$

$$C_0 = \lambda_{p0}^{(2)} \left[ \frac{p_2}{4\pi \rho_0} \right],$$

$$C_1 = \lambda_{p1}^{(2)} \left[ \frac{p_2}{8\pi \rho_0} \right].$$

These relations involve the frame transformation factor  $p_2$  and the constant nuclear matter density  $\rho_0$ .

#### APPENDIX C: ISOSPIN COMPONENTS OF THE EL TERM

As given by Eq. (3.1), the EL correlation term has isospin operators in the numerator and denominator, i.e.,

$$X_p = -\frac{\alpha}{3} (\xi_p)^2 \left[ 1 + \frac{\alpha}{3} \xi_p \right]^{-1}, \quad (\text{C1})$$

where

$$\xi_p = \lambda_{p0}^{(1)} \rho(r) + (\boldsymbol{\phi} \cdot \mathbf{T}) \lambda_{p1}^{(1)} \left[ \frac{\Delta \rho(r)}{2T_0} \right].$$

Our goal here is to express the complete isospin dependence of  $X_p$  in the form given by Eq. (3.2), and thereby identify the coefficients  $X_{p0}$ ,  $X_{p1}$ , and  $X_{p2}$  that multiply the corresponding zeroth, first, and second powers of  $\boldsymbol{\phi} \cdot \mathbf{T}$ .

To accomplish this goal, we first rewrite the denominator of Eq. (C1) as

$$\left[ 1 + \frac{\alpha}{3} \xi_p \right]^{-1} = L (1 + \beta \boldsymbol{\phi} \cdot \mathbf{T})^{-1}, \quad (\text{C2})$$

where

$$L^{-1} = \left[ 1 + \frac{\alpha}{3} \lambda_{p0}^{(1)} \rho \right]$$

and

$$\beta = \frac{\alpha}{3} L \lambda_{p1}^{(1)} (\Delta \rho / 2T_0).$$

Next, we use the binomial expansion

$$(1 + \beta \boldsymbol{\phi} \cdot \mathbf{T})^{-1} = \sum_{n=0} (-\beta \boldsymbol{\phi} \cdot \mathbf{T})^n. \quad (\text{C3})$$

In this form, we can use the results of Appendix A to express  $(\phi \cdot \mathbf{T})^n$  as powers of order two and lower. That is, by using Eq. (A3) for  $(\phi \cdot \mathbf{T})^n$  in Eq. (C3), we can write

$$(1 + \beta \phi \cdot \mathbf{T})^{-1} = A(\phi \cdot \mathbf{T})^2 + B(\phi \cdot \mathbf{T}) + C, \quad (\text{C4})$$

where

$$\begin{aligned} A &= \beta^2 + \sum_{n=3} (-\beta)^n a_n, \\ B &= -\beta + \sum_{n=3} (-\beta)^n b_n, \\ C &= 1 + \sum_{n=3} (-\beta)^n c_n. \end{aligned} \quad (\text{C5})$$

Now by using Eqs. (C4) and (C2) to rewrite (C1), we obtain powers of  $\phi \cdot \mathbf{T}$  to order four and lower. Again using Eq. (A3) to reduce the third and fourth powers, we finally obtain the fully reduced form of  $X_p$ . The resulting coefficients  $X_{pi}$  that multiply the operators  $(\phi \cdot \mathbf{T})^i$  for  $i=0,1,2$  are the following:

$$\begin{aligned} X_{pi} &= -\frac{\alpha}{3} L \left[ (\lambda_{p0}^{(1)})^2 \eta_i + \left[ \lambda_{p0}^{(1)} \lambda_{p1}^{(1)} \frac{\rho \Delta \rho}{T_0} \right] \mu_i \right. \\ &\quad \left. + \left[ \lambda_{p1}^{(1)} \frac{\Delta \rho}{2T_0} \right]^2 \nu_i \right], \end{aligned} \quad (\text{C6})$$

where in terms of the coefficients  $A$ ,  $B$ , and  $C$ ,

$$\begin{aligned} \eta_0 &= C, \quad \mu_0 = T_0(T_0 + 1)A, \\ \nu_0 &= T_0(T_0 + 1)(B - 2A), \\ \eta_1 &= B, \quad \mu_1 = [T_0(T_0 + 1) - 1]A + C, \\ \nu_1 &= T_0(T_0 + 1)(B - A) + 2A - B, \\ \eta_2 &= A, \quad \mu_2 = B - 2A, \\ \nu_2 &= [T_0(T_0 + 1) + 3]A - 2B + C. \end{aligned} \quad (\text{C7})$$

From the expressions given in Eqs. (C5), we see that if we consider  $X_{pi}$  to order  $(\Delta \rho)^2$ , the  $\eta$ ,  $\mu$ , and  $\nu$  coefficients become  $\eta_0=1$ ,  $\eta_1=-\beta$ ,  $\eta_2=\beta^2$ ;  $\mu_0=0$ ,  $\mu_1=1$ ,  $\mu_2=-\beta$ ;  $\nu_0=0$ ,  $\nu_1=0$ ,  $\nu_2=1$ . Inserting these values into Eq. (C6), we obtain the expressions for the isospin components of  $X_p$  given by Eqs. (3.3).

\*Present address: Los Alamos National Laboratory, Los Alamos, NM 87545.

- <sup>1</sup>M. D. Cooper, H. W. Baer, R. Bolton, J. D. Bowman, F. Cverna, N. S. P. King, M. Leitch, J. Alster, A. Doron, A. Erell, M. A. Moinester, E. Blackmore, and E. R. Siciliano, Phys. Rev. Lett. **52**, 1100 (1984).
- <sup>2</sup>M. J. Leitch, E. Piasetzky, H. W. Baer, J. D. Bowman, R. L. Burman, B. J. Dropesky, P. A. M. Gram, F. Irom, D. Roberts, G. A. Rebka, Jr., J. N. Knudson, J. R. Comfort, V. A. Pinnick, D. H. Wright, and S. A. Wood, Phys. Rev. Lett. **54**, 1482 (1985); I. Navon, M. J. Leitch, D. A. Bryman, T. Numao, P. Schlatter, G. Azuelos, R. Poutissou, R. A. Burnham, M. Hasinoff, J. M. Poutissou, J. A. Macdonald, J. E. Spuller, C. K. Hargrove, H. Mes, M. Blecher, K. Gotow, M. Moinester, and H. Baer, *ibid.* **52**, 105 (1984).
- <sup>3</sup>M. Ericson and T. E. O. Ericson, Ann. Phys. (N.Y.) **36**, 323 (1966).
- <sup>4</sup>M. Krell and T. E. O. Ericson, Nucl. Phys. **B11**, 521 (1969).
- <sup>5</sup>M. Thies, Phys. Lett. **63B**, 43 (1976).
- <sup>6</sup>K. Stricker, H. McManus, and J. A. Carr, Phys. Rev. C **19**, 929 (1979); K. Stricker, J. A. Carr, and H. McManus, *ibid.* **22**, 2043 (1980); J. A. Carr, H. McManus, and K. Stricker-Bauer, *ibid.* **25**, 952 (1982).
- <sup>7</sup>J. M. Eisenberg, J. Hufner, and E. J. Moniz, Phys. Lett. **47B**, 381 (1973).
- <sup>8</sup>S. Barshay, G. E. Brown, and M. Rho, Phys. Lett. **32**, 787 (1974).
- <sup>9</sup>R. Seki and K. Masutani, Phys. Rev. C **27**, 2799 (1983).
- <sup>10</sup>G. A. Miller, Phys. Rev. Lett. **53**, 2008 (1984).
- <sup>11</sup>M. J. Leitch, H. W. Baer, J. D. Bowman, M. D. Cooper, E. Piasetzky, U. Sennhauser, H. J. Ziock, F. Irom, P. B. Siegel, and M. A. Moinester, Phys. Rev. C **33**, 278 (1986).
- <sup>12</sup>J. L. Ullmann, P. W. F. Alons, J. J. Kraushaar, J. M. Mitchell, R. J. Peterson, R. A. Ristinen, J. N. Knudson, J. R. Comfort, H. W. Baer, J. D. Bowman, M. D. Cooper, D. H. Fitzgerald, F. Irom, M. J. Leitch, and E. Piasetzky, Phys.

Rev. C **33**, 2092 (1986).

- <sup>13</sup>T. Karapiperis and M. Kobayashi, Phys. Rev. Lett. **54**, 1230 (1985).
- <sup>14</sup>W. B. Kaufmann and W. R. Gibbs, Phys. Rev. C **28**, 1286 (1983).
- <sup>15</sup>M. B. Johnson and E. R. Siciliano, Phys. Rev. C **27**, 730 (1983).
- <sup>16</sup>M. B. Johnson and E. R. Siciliano, Phys. Rev. C **27**, 1647 (1983).
- <sup>17</sup>S. J. Greene, C. J. Harvey, P. A. Seidl, R. Gilman, E. R. Siciliano, and M. B. Johnson, Phys. Rev. C **30**, 2003 (1984).
- <sup>18</sup>M. B. Johnson, Phys. Rev. C **22**, 192 (1980).
- <sup>19</sup>G. A. Miller and J. E. Spencer, Ann. Phys. (N.Y.) **100**, 562 (1976); Phys. Rev. C **22**, 2639 (1980); M. Koren, Ph.D. thesis, MIT, 1969 (unpublished).
- <sup>20</sup>H. A. Bethe and M. B. Johnson, Los Alamos National Laboratory Report LA-5842-MS, 1975.
- <sup>21</sup>G. E. Brown, B. K. Jennings, and V. I. Rostokin, Phys. Rep. **50C**, 227 (1979).
- <sup>22</sup>M. B. Johnson and H. A. Bethe, Nucl. Phys. **A305**, 418 (1978).
- <sup>23</sup>E. Oset, D. Strottman, M. J. Vicente-Vacas, and Ma Wei-Hsing, Nucl. Phys. **A408**, 461 (1983).
- <sup>24</sup>Program SAID (Scattering Analysis Interactive Dialin), R. A. Arndt, Virginia Polytechnic Institute and State University, Solution C5, August, 1984.
- <sup>25</sup>Rubin H. Landau and Malcolm McMillan, Phys. Rev. C **8**, 2094 (1973).
- <sup>26</sup>E. Friedman and A. Gal, Nucl. Phys. **345**, 457 (1980).
- <sup>27</sup>G. Baym and G. E. Brown, Nucl. Phys. **A247**, 345 (1975).
- <sup>28</sup>P. Delorme and M. Ericson, Phys. Lett. **60B**, 451 (1976).
- <sup>29</sup>G. E. Brown and W. Weise, Phys. Rep. **22**, 279 (1975); E. Oset, H. Toki, and W. Weise, *ibid.* **83**, 281 (1982).
- <sup>30</sup>G. E. Brown, in *Spin Excitations in Nuclei*, edited by F. Petrovich *et al.* (Plenum, New York, 1984), p. 233.
- <sup>31</sup>K. Holinde, Phys. Rep. **68**, 122 (1981).
- <sup>32</sup>C. W. deJager, H. deVries, and C. deVries, At. Data Nucl.

- Data Tables 14, 479 (1974).
- <sup>33</sup>B. M. Preedom, S. H. Dam, C. W. Darden III, R. D. Edge, D. J. Malbrough, T. Marks, R. L. Burman, M. Hamm, M. A. Moinester, R. P. Redwine, M. A. Yates, F. E. Bertrand, T. P. Cleary, E. E. Gross, N. W. Hill, C. A. Ludemann, M. Blecher, K. Gotow, D. Jenkins, and F. Milder, *Phys. Rev. C* **23**, 1134 (1981).
- <sup>34</sup>P. W. F. Alons, M. J. Leitch, and E. R. Siciliano, submitted to *Phys. Rev. C*.
- <sup>35</sup>A. Altman, R. R. Johnson, U. Wienands, N. Hessey, B. M. Barnett, B. M. Forster, N. Grion, D. Mills, F. M. Rozon, G. R. Smith, R. P. Trelle, D. R. Gill, G. Sheffer, and T. Anderl, *Phys. Rev. Lett.* **55**, 1273 (1985).
- <sup>36</sup>W. J. Gerace, W. J. Leonard, and D. A. Sparrow, University of Massachusetts report, 1986.
- <sup>37</sup>R. A. Eisenstein and G. A. Miller, *Comput. Phys. Commun.* **11**, 95 (1976).
- <sup>38</sup>D. H. Fitzgerald, H. W. Baer, J. D. Bowman, F. Irom, N. S. P. King, M. J. Leitch, E. Piasetzky, W. J. Briscoe, M. E. Sadler, K. J. Smith, and J. N. Knudson, *Phys. Rev. C* (in press).
- <sup>39</sup>M. Beiner, H. Flocard, Nguyen van Giai, and P. Quentin, *Nucl. Phys.* **A238**, 29 (1975).
- <sup>40</sup>P. Roman, *Advanced Quantum Theory* (Addison-Wesley, Reading, Mass., 1965), p. 550.